Numerical analysis of vibroacoustic beamforming gains for acoustic source detection inside a pipe conveying turbulent flow

Laurent Maxit, Mahmoud Karimi, Oriol Guasch, Frédéric Michel

Numerical analysis of vibroacoustic beamforming gains for acoustic source detection inside a pipe conveying turbulent flow

Laurent Maxit[1], Mahmoud Karimi[2], Oriol Guasch [3], Frédéric Michel [4]

1. Univ Lyon, INSA Lyon, LVA, 25 bis, av. Jean Capelle, 69621, Villeurbanne Cedex, France.
e-mail: laurent.maxit@insa-lyon.fr (corresponding author)
2. Centre for Audio, Acoustics and Vibration, University of Technology Sydney, Sydney, Australia
3. GTM - Grup de recerca en Tecnologies Mèdia, La Salle, Universitat Ramon Llull, C/ Quatre Camins 30, 08022 Barcelona, Catalonia, Spain
4. CEA, DES, IRESNE, Nuclear Technology Department, Cadarache F-13108 Saint-Paul-Lez-Durance, France

Abstract:

This study concerns a monitoring technique based on vibration measurements for identifying the presence of an acoustic source in a fluid-filled pipe conveying turbulent flow. In such situation, the source-induced vibrations can be smeared with the flow-induced vibrations, which hinders detecting the presence of the source. To increase the signal-to-noise ratio (SNR), beamforming techniques can be applied to the vibrations measured by an array of accelerometers mounted on the pipe. However, the current problem is more complex and challenging than most typical beamforming applications due to strong fluid-structure coupling and to the presence of resonant modes and internal flow excitations. Numerical vibroacoustic methods are presented to predict the vibratory response of a pipe excited by a monopole source and/or a turbulent boundary layer (TBL). The cross-spectral matrices of the computed radial accelerations induced by the monopole source to be detected and by the TBL are used for assessing the performance of two vibroacoustic beamforming techniques. The array gains using both, the conventional and the MaxSNR beamforming approaches are estimated. Results indicate superior performance of the MaxSNR, which leads to significantly higher array gain.

Keywords: leak detection, beamforming, array gain, vibroacoustic modeling, heavy fluid loading, turbulent boundary layer

1. Introduction

This paper deals with numerical simulations of beamforming techniques for the detection of an acoustic source located inside a pipe that also conveys a turbulent flow. The focus is on the detection of the acoustic source, that is, on the ability to identify the presence or absence of the

source taking into account that the sound it radiates will be masked by the background noise induced by the turbulent flow. It should be emphasized that detection does not necessarily mean localization. A source can be detected without localization if a significant increase of the beamforming output signals is observed. The localization of the source is another potential of beamforming techniques, which could be implemented in case of interest once the source has been detected. The beamforming methods suitable for source detection are not necessarily efficient for source localization, as it will be shown in the case of MaxSNR beamforming. This paper essentially focuses on analyzing the capability of beamforming methods to increase the signal to noise ratio for source detection. To that goal, numerical simulations are used to compute the accelerometer responses induced by the acoustic source to be detected and also by background noise generated by the turbulent flow. Resorting to numerical simulations allows one to perform virtual experiments and easily control all system parameters to thoroughly investigate their influence on the system response. As opposed, conducting real experiments to try to derive the parametric system dependence would be extremely expensive and time consuming. Therefore, this work complements the real experimental work in [1] and sheds new light on its results. In [1], a set-up was built to study and improve beamforming techniques for the early detection of sodium leaks in the steam generator unit (SGU) of a liquid sodium fast reactor (SFR) [2]. In this paper, we provide supplementary numerical evidence and theoretical explanations to the outcomes in [1], which can be of interest to more general problems of acoustic source detection in pipes with a noisy, turbulent background excitation.

Sodium leaks can result in severe reactor damage and many investigators have examined active [3] and passive [4] means to detect them. The passive techniques rely on the fact that the leak generates acoustic noise due to substantial sodium-water chemical reaction. As the time it takes for the acoustic waves to propagate from the leak to the microphones on the SGU pipe inner surface is very short, acoustic techniques can be implemented for fast leak detection. Nevertheless, the latter are highly sensitive to the background noise from the sodium and water flows as well as to the noise from the boiling water and vibrations induced by the pumps. Kim et al. [6] analysed the noise generated by the sodium-water reaction. They demonstrated that a small leak at a rate of 0.4 to 0.6 g s^{-1} could produce a wide band noise from 1 to 200 kHz, which could be detected using a single sensor. Since the signal-to-noise ratio (SNR) can be lower than 0 dB for microleaks, advanced signal processing techniques are required for proper localization. Hayashi et al. [5] applied the so-called twice-squaring method to a signal containing

experimental leak noise and background noise from real steam generators. They showed that their method can detect a leak noise with a SNR as low as -20 dB.

Beamforming techniques using an array of microphones are popular as they can increase the SNR of the leak signal, which is usually masked by the SGU background noise ([2, 6]). For instance, an acoustic leak detection method based on the so-called delay-and-sum beamformer was introduced by Chikazawa et al. [3, 7]. It was assumed that the background noise was uniformly distributed, unlike the sodium-reaction noise source, which was considered to be localized. The proposed approach could differentiate the leak source from the SGU background noise even when they had very close magnitudes. The numerical results were validated by an experiment in a water tank in [7].

A different vibroacoustic beamforming methodology was suggested by Moriot [8], which relies on measuring vibration data on the external surface of the SGU and on steering vectors taking the fluid-structure interaction into account. Conventional beamforming (sometimes called Bartlett beamforming) was used by Moriot et al. [9, 10] to detect a leak in the SGU, under the assumption of uncorrelated background noise between the sensors. To approximate the leakage problem, the source was simulated as an acoustic monopole and the SGU was modelled either as an infinite plate in [9], or as an infinite cylindrical shell in [10]. It was confirmed that to localize the monopole source one can perform vibroacoustic beamforming by mounting a linear array of accelerometers on the external surface of the structure. However, the main purpose of beamforming is to achieve a high SNR. The array gain is generally used to quantify it. The array gain is defined as the ratio between the SNR at the beamforming output and that of the reference sensor (i.e., the sensor with the highest SNR). To improve the detection accuracy and to limit the sensitivity of the array to false alarms, a threshold criterion can be imposed at the beamforming output instead of the reference sensor. Although the numerical and experimental work in [10] was promising in terms of array gain improvement, simple academic models (an infinite plate or a cylindrical shell) were used to obtain the numerical results. Furthermore, it was assumed that background noise was uncorrelated. Unfortunately, this last hypothesis is hardly met in practice and observations reveal that the background noise can be significantly correlated at high flow speeds. This can decrease the array gain and deteriorate the beamforming performance. In addition, the experiment in [10] was only conducted for a limited number of discrete frequencies for the harmonic monopole source, while the water-sodium reaction is known to be wideband in spectrum [6].

Kassab et al. [1] further investigated vibroacoustic beamforming using the experimental set-up of [9], [10]. The mock-up comprised a cylindrical pipe filled with water (used instead of sodium for practical reasons) connected to a hydraulic circuit by two flanges (see Fig. 1a). The source to be detected was represented by a hydrophone in transmission mode located inside the pipe, and the background noise due to turbulence was controlled by changing the flow rate. A vibroacoustic beamforming was applied to the accelerometers mounted on the pipe to strengthen the source signal and filter the background noise, as much as possible. The conventional beamforming was proved to be totally inaccurate in the band [1 kHz - 5 kHz] at high flow rates (i.e., 140 l s^{-1}). This was attributed to the strong coherence of the vibration signals induced by the turbulent flow, which contradicts the underlying assumption of spatially uncorrelated background noise of conventional beamforming, mentioned before. On the other hand, the MaxSNR beamforming technique [11], which is not relying on such hypothesis, exhibited remarkable gains (about 10 to 25 dB) for different positions of the source. The spatial coherence of the accelerometers' signals induced by an internal turbulent flow has been recently investigated in [12] using numerical modelling.

In this work, we have developed further numerical models that mimic the above-mentioned laboratory mock-up [1] for better understanding the performance of the conventional and MaxSNR beamforming techniques. The numerical models include the coupling between the pipe and the flanges as well as the coupling between the pipe and the internal fluid (water). The models also allow us to simulate the pipe vibrations excited by a monopole source (i.e. the source to be detected) and/or by an inner turbulent flow (i.e. the background noise). The performance of the two different beamforming techniques is evaluated by computing the beamforming gains from the cross-spectral acceleration matrix of an array of sensors.

The main advantage of numerical simulations for our problem, as compared to the experiments in [1], is that we can control all system parameters and more easily comprehend their influence. For instance, and as said above, in the experiments the source to be detected was simulated by a hydrophone in emitter mode. However, it was neither possible to know its precise directivity nor the vibration the hydrophone directly transmitted to the array through its mounting device. In contrast, in the simulations the monopole can be perfectly defined, and one can get rid of such potential spurious data. As another example, even if special care is taken in experiments to avoid unwanted system noise sources by using acoustic decoupling tanks, a perforated plate flow conditioner, rubber seals or a suspended pipe, it becomes very difficult to evaluate the importance of turbulent flow noise as compared to that generated by other uncontrolled

undesirable sources. As opposed, in the numerical simulations we just consider a model for the wall pressure fluctuations of the turbulent boundary layer (TBL) so that it becomes easier to analyse its impact. An extra advantage is that the numerical model also allows one to carry out a parametric analysis by modifying e.g., the radius, thickness and material properties of the pipe, or the source position and the background noise level. Analogous experiments will be extremely costly from an economic and time duration point of view.

The methodology proposed in this paper can be summarised as follows. First, numerical simulations are used to compute the cross-spectral density matrix of the virtually measured accelerations by the sensor array when the fluid filled pipe is excited either, by the acoustic source to be detected, or by the turbulent boundary layer. From these virtual experiments, the performances of different beamforming treatments are then analysed with respect to the vibroacoustic characteristics of the fluid filled pipe. Finally, a parametric study is performed to observe the sensitivity of the beamforming performance to the variations of physical and geometrical parameters of the considered system. However, as many parameters can be studied, in this work we will concentrate on those more relevant to the experimental work in [1], namely the source position, the damping of the system, the flow speed and the frequency band of analysis. It is apparent that numerical modelling implies simplification, but it can be very helpful for understanding the underlying physics of the problem.

The remaining of this paper is organized as follows. In section 2, we present the hypotheses and principles of the numerical model employed to compute the accelerations in the pipe surface induced by the turbulent flow and by the monopole source. The theoretical core of the model was recently presented in [12] and validated through the independent experiments in [13]. An extension is proposed herein to calculate the shell vibrations induced by the monopole source inside the fluid. Section 3 reviews the basics of the conventional and MaxSNR beamforming techniques and introduce the reference sensor and the array gain. The computed accelerations on the pipe due to the monopole and TBL sources are analysed in section 4, whereas the performance of the two beamforming techniques is investigated in section 5 for both, narrow band and wide band frequency excitation. Conclusions close the paper in section 6.

2. Test case and numerical model

2.1 Description of the test case

The experimental set-up in [1] has been considered, see Fig. 1a. The mock-up consists of a cylindrical pipe made of stainless steel representing the shell of the steam generator. To ease

manipulation and enhance safety, the pipe was filled with water rather than sodium. The test section of the pipe was linked to the hydraulic circuit by two stiff flanges. A 4 meter-long pipe was used to stabilize the turbulent flow upstream of the test section, while a 1.5 meter-long pipe was employed for the discharge before the acoustic balloon. These two pipes have the same dimensions than the test one.

In the present numerical study, the mechanical system in Fig. 1a will be simplified and represented by an infinite thin cylindrical shell coupled with two ring stiffeners as shown in Fig. 1b. The radius R and thickness h of the shell are 109 mm and 8 mm, respectively. The flanges are modelled as ring stiffeners with rectangular cross-section 0.04 m (width) $\times$ 0.06 m (height). The distance between the two ring stiffeners is 3.1 m, which corresponds to the distance between the mid-surfaces of the two flanges of the experimental test section. Both the pipe and flanges are made of stainless steel, whose material properties are chosen as $\rho = 7800\ \mathrm{kg\ m^{-3}}$ for the density, $E = 185\ \mathrm{GPa}$, for the Young mudulus, $\nu = 0.33$ for the Poisson's ratio, and $\eta = 0.001$ for the damping loss factor. The density, speed of sound and the loss factor for the water in the pipe are $\rho_0 = 1000\ \mathrm{kg\ m^{-3}}$, $c_0 = 1500\ \mathrm{m\ s^{-1}}$ and $\eta_0 = 0.001$. The water flow rate is 140 l $\mathrm{s^{-1}}$ for a flow speed of $U_0 =$ 4.5 m $\mathrm{s^{-1}}$, which corresponds to the experimental value. As the flow speed is small compared to the speed of sound, the effects of convection will be neglected.

The cylindrical shell dynamics will be obtained from the Flügge model [14], whereas acoustic wave propagation will be accounted for by the Helmholtz equation [15]. Only the coupling along the radial direction between the shell and the stiffener will be considered. The ring stiffener will be represented by a rod of circular curvature, as described in [12, 16]. A cylindrical coordinate system (x, r, θ) is adopted, as in Fig. 1b.

The source to be detected will consist of a monopole placed inside the cylindrical shell and the background noise will be induced by the TBL of the turbulent water flow, as illustrated in Fig. 1b. An accelerometer array on the shell is considered for performing the vibroacoustic beamforming. Different geometries of the array as well as different accelerometers spacing could be easily considered in the present approach. However, in order to mimic the laboratory experiment in [1] and avoid additional complexity, we have chosen an array of 25 sensors fixed on the cylindrical generator at $\theta_i = 0°$ (see Fig. 1a). The spacing between accelerometers is $\Delta x = 4$ cm and the first accelerometer is positioned at 15 cm from the stiffener upstream of the flow. The axial position of the i-th accelerometer is therefore given by $x_i = 0.15 +$

$0.04(i-1)$ for $i \in \{1,..,25\}$. The frequency band of analysis is set to [200 Hz – 2000 Hz] with a frequency resolution of 4 Hz.

The virtual experiments to assess the performance of the beamforming involves computing the cross-spectrum density (CSD) of the radial acceleration measured by the array when the mechanical system is excited either by the monopole source or by the TBL. Section 2.2 describes how to estimate the vibratory response of the mechanical system excited by the TBL by exploiting the reciprocity principle, while section 2.3 focuses on the calculation of the vibration response induced by the monopole source.

2.2 Vibration response of the shell excited by the turbulent boundary layer

Let us consider a fluid-filled shell coupled to the two ring stiffeners and excited by a TBL. As said, the flow speed is assumed low compared to the speed of sound, and the TBL is considered to be stationary, homogeneous and fully developed [17]. The CSD of the wall pressure field (WPF) induced by the TBL, ϕ_{pp}, is estimated from the Chase 1987 model [18, 19] and the TBL parameter values are such that the TBL thickness equals the shell radius, whereas the convective and friction velocity are respectively taken as $U_c = 0.7U_0$, and $U_\tau = 0.032U_0$ (see [13]).

It should be noted that the theoretical foundations of the model to be used below were recently presented in detail in [12] and validated through the independent experiments in [13]. For completeness, the outline of the model is presented herein for the case of the shell excited by the TBL. An extension for the shell excited by a monopole source is then proposed in section 2.3. The readers are referred to [12] for further information and deeper insight on the theoretical derivations.

In what follows, a Fourier analysis [15, 20, 21] will be employed. For a generic function f representing either the shell displacements or the acoustic pressure, the series decomposition along the circumference $\tilde{f}$ followed by the space Fourier transform about the *x*-axis $\tilde{\tilde{f}}$ are given by:

$$\begin{cases} \tilde{f}(x,n) = \dfrac{1}{2\pi}\displaystyle\int_0^{2\pi} f(x,\theta) e^{-\mathrm{i}k_x x}\, e^{-\mathrm{i}n\theta} d\theta\,, & \forall (x,n) \in \mathbb{R}\times\mathbb{Z}, \\ \tilde{\tilde{f}}(k_x,n) = \dfrac{1}{2\pi}\displaystyle\int_{-\infty}^{+\infty}\int_0^{2\pi} f(x,\theta) e^{-\mathrm{i}k_x x}\, e^{-\mathrm{i}n\theta}\, d\theta dx, & \forall (k_x,n) \in \mathbb{R}\times\mathbb{Z}. \end{cases} \tag{1}$$

Considering the formulation of the vibroacoustic problem in the Fourier domain (k_x, n), the CSD of the computed radial acceleration ("virtual measurement") between the *i*-th and *j*-th sensors, S_{ij}^n induced by the TBL background noise can be obtained as (see [12, 22, 23]):

$$S_{ij}^n(\omega) = \frac{\omega^4}{R} \sum_{n=-\infty}^{+\infty} \int_{-\infty}^{+\infty} \tilde{\tilde{H}}_w^{\omega\,*}(x_i, \theta_i, k_x, n, \omega) \phi_{pp}\left(k_x, \frac{n}{R}, \omega\right) \tilde{\tilde{H}}_w^{\omega}\left(x_j, \theta_j, k_x, n, \omega\right) dk_x, \quad (2)$$

where * stands for complex conjugation, ϕ_{pp} is the CSD of the WPF induced by the TBL, $\tilde{\tilde{H}}_w^{\omega}$ are the sensitivity functions and (x_i, θ_i) and (x_j, θ_j) are the cylindrical coordinates of the *i-th* and *j-th* sensors, respectively. Using the reciprocity principle in [24], $\tilde{\tilde{H}}_w^{\omega}$ can be computed as,

$$\tilde{\tilde{H}}_w^{\omega}(x, \theta, k_x, n, \omega) = \frac{R}{2\pi} \int_{-\infty}^{+\infty} \int_{0}^{2\pi} H_w(\tilde{x}, \tilde{\theta}, x, \theta, \omega) \mathrm{e}^{-\mathrm{i}k_x \tilde{\mathrm{x}}} e^{-\mathrm{i}n\tilde{\theta}} d\tilde{\mathrm{x}}\, d\tilde{\theta} \quad (3)$$

In Eq. (3), $H_w(\tilde{x}, \tilde{\theta}, x, \theta, \omega)$ stands for the radial displacement of the shell at point $\tilde{M}$ of coordinates $(\tilde{x}, \tilde{\theta})$ when a unit harmonic radial point force of angular frequency ω is applied at point M of coordinates (x, θ) (see Fig. 1b). From Eq. (1), one can interpret the sensitivity functions $\tilde{\tilde{H}}_w^{\omega}$ in Eq. (3) as the product between the shell radius and the Fourier transform of the shell radial displacement field W (i.e., $\tilde{\tilde{W}}$ in the (k_x, n) space), when the shell is excited by a unit radial point force at point M. That is $\tilde{\tilde{H}}_w^{\omega} = R\tilde{\tilde{W}}$. Therefore, to calculate $\tilde{\tilde{H}}_w^{\omega}$, it suffices to excite the system with a radial harmonic point force at $M(x, \theta)$ with an oscillating angular frequency ω. By applying the 2D Fourier transform of Eq. (1) to the Flügge, Helmholtz, and Euler equations [25] that describe the behaviour of the coupled fluid-structure system, the spectral radial displacement of the shell, $\tilde{\tilde{W}}$, can be obtained from [12, 26, 27],

$$\tilde{\tilde{W}} = \gamma \tilde{\tilde{F}}_w \frac{\tilde{\tilde{Z}}_{uu} \tilde{\tilde{Z}}_{vv} - \left(\tilde{\tilde{Z}}_{uv}\right)^2}{\tilde{\tilde{\Delta}}}. \quad (4)$$

Here, $\tilde{\tilde{Z}}_{uu}$, $\tilde{\tilde{Z}}_{vv}$, $\tilde{\tilde{Z}}_{uv}$ are the components of the spectral Flügge matrix, $\tilde{\tilde{\Delta}}$ is its determinant including the spectral fluid loading impedance, and γ is a constant depending on the shell characteristics. A full description of these parameters and on how to derive Eq. (4) is provided in [12] with the same notation than in the present paper.

On the other hand, as the mechanical forces applied on the fluid filled shell consist in the external radial point force applied at $M(x, \theta)$ and the radial line forces exerted by the ring stiffeners on the shell, the total spectral radial force can be written as ([12]),

$$\tilde{\tilde{F}}_w = \tilde{\tilde{F}}_e + \tilde{F}_1^1 e^{-\mathrm{i}k_x x_1} + \tilde{F}_2^1 e^{-\mathrm{i}k_x x_2}, \tag{5}$$

where $\tilde{\tilde{F}}_e$ corresponds to the external excitation. In the case of a unit radial oscillating point force applied at $M(x\,,\theta)$ we get ([26])

$$\tilde{\tilde{F}}_e = \frac{e^{-\mathrm{i}(n\theta + k_x x)}}{2\pi R}. \tag{6}$$

$\tilde{F}_1^1$ and $\tilde{F}_2^1$ in Eq. (5) are the circumferential radial forces respectively applied at the shell junctions #1 and #2 by the stiffeners. Their values can be calculated with the circumferential admittance approach (CAA) [12, 26], which partitions the system in two subsystems: the fluid filled shell on the one hand and the ring stiffeners on the other one (see Fig. 2). The CAA characterizes each subsystem by its circumferential admittance at the junctions. For the fluid filled shell, the admittances can be deduced from an inverse Fourier transform along k_x of the spectral displacements of Eq. (4). For the ring stiffeners, they can be calculated analytically (see [12, 16]). Once the shell and stiffeners' admittances and the free displacements induced by the external excitation have been computed, the circumferential coupling forces between the shell and stiffeners, $\tilde{F}_1^1$ and $\tilde{F}_2^1$, can be obtained. The details of these CAA calculations are fully described in [12]. Injecting the spectral forces from Eq. (5) into Eq. (4) for the spectral radial displacement $\tilde{\tilde{W}}$, finally allows one to deduce the sensitivity functions as $\tilde{\tilde{H}}_w^{\omega} = R\tilde{\tilde{W}}$.

In summary, the CSD of the radial displacement between sensors #*i* and #*j* due to the TBL excitation can be estimated from Eq. (2) using the sensitivity functions $\tilde{\tilde{H}}_w^{\omega}$ (obtained with the CAA method) and the CSD of the WPF, ϕ_{pp}, of the Chase model [18].

2.3 Vibration response of the shell excited by the monopole source

Next, let us compute the CSD of the radial acceleration between the *i*-th and *j*-th sensors, S_{ij}^{s} when the fluid-filled shell with its two stiffeners is excited by a monopole source located inside the fluid at $S(x_s, r_s, \theta_s)$ (see Figs. 1b and 2a). The monopole is characterized by its mass flow acceleration q_s (kg s^{-2}) and has harmonic dependence with time $e^{\mathrm{i}\omega t}$.

The spectral radial displacement of the shell can still be computed from Eq. (4) and the CAA will provide the circumferential coupling forces between the shell and stiffeners, $\tilde{F}_1^1$ and $\tilde{F}_2^1$ when the system is excited by the monopole source. In this case, the external mechanical point excitation in Eq. (6) gets replaced with the acoustic one [28],

$$\tilde{\tilde{F}}_e = \frac{q_s e^{-\mathrm{i}(n\theta_s + k_x x_s)}}{2\pi k_r R} \frac{J_n(k_r r_s)}{J'_n(k_r R)}, \tag{7}$$

where J_n is the Bessel function of order n, J'_n represents its derivative with respect to its argument, and k_r the radial wavenumber defined by

$$k_r = \begin{cases} \sqrt{k_0^2 - k_x^2} & \text{if } |k_x| \le k_0, \\ -\mathrm{i}\sqrt{k_x^2 - k_0^2} & \text{otherwise,} \end{cases}$$

with k_0 being the acoustic wavenumber.

The spectral radial displacement of the fluid-filled shell coupled to the ring stiffeners is then computed by substituting $\tilde{\tilde{F}}_e$ from Eq. (7) and the new $\tilde{F}_1^1$ and $\tilde{F}_2^1$ into Eq. (5) and then into Eq. (4). The radial displacement in the physical space due to the monopole is finally recovered from the inverse Fourier transform,

$$W(x, \theta, \omega) = \frac{1}{2\pi} \sum_{n=-\infty}^{\infty} e^{\mathrm{i}n\theta} \int_{-\infty}^{\infty} \tilde{\tilde{W}}(k_x, n, \omega)\, e^{\mathrm{i}k_x x} dk_x. \tag{8}$$

It should be noted that the inverse Fourier transform in Eq. (8) is calculated numerically after reducing the infinite wavenumber space to the finite space $\left[-\bar{k}_x, \bar{k}_x\right] \times [-\bar{N}, \bar{N}]$, where $\bar{k}_x$ and $\bar{N}$ are cut-off wavenumber/circumferential orders judiciously chosen to avoid the loss of significant contributions. The CSD of the radial acceleration virtually measured between the *i*-th and *j*-th sensors induced by the monopole, S_{ij}^s, is then given by,

$$S_{ij}^s(\omega) = \omega^4\, W(x_i, \theta_i, \omega) W^*\left(x_j, \theta_j, \omega\right). \tag{9}$$

3. Conventional and MaxSNR beamforming techniques

In this section, we briefly review the principles of classical and MaxSNR beamforming techniques ([29-33]). We also introduce different quantities that are required for the analysis of the results in section 5.

3.1 Definition of beamforming elements

The cross-spectral matrix of the signals virtually measured by the accelerometers at angular frequency ω is denoted by $\mathbf{\Gamma}(\omega)$. For an array of n accelerometers, $\mathbf{\Gamma}$ is an $n \times n$ square matrix where the entry in the *i*-th row and the *j*-th column corresponds to the CSD function of the accelerations between sensors *i*-th and *j*-th at frequency ω, i.e.,

$$\mathbf{\Gamma}(\omega) = \left[\mathrm{S}_{ij}(\omega)\right]_{n \times n}. \tag{10}$$

Assuming that the signals induced by the acoustic source in the pipe are independent from those generated by the background noise, matrix $\mathbf{\Gamma}$ can be split up such that,

$$\mathbf{\Gamma} = \mathbf{\Gamma}^s + \mathbf{\Gamma}^n \,, \tag{11}$$

where $\mathbf{\Gamma}^s$ is the cross-spectral matrix of the accelerations only due to the monopole source and $\mathbf{\Gamma}^n$ is the cross-spectral matrix of the accelerations only produced by the TBL background noise.

Applying a spatial filter to the signals received by the array of sensors is the basic principle of a beamforming technique. We herein introduce a pre-filtering stage before implementing the main one. To do this, an independent analysis of each individual signal is required. Let us define the SNR of the *i*-th sensor at the angular frequency ω as follows,

$$\mathrm{SNR}_i(\omega) = 10\log_{10}\left(\frac{S_{ii}^s(\omega)}{S_{ii}^n(\omega)}\right), \tag{12}$$

where S_{ii}^s is the auto-spectral density (ASD) function of the acceleration measured by *i*-th sensor in the sole presence of the monopole source (given by Eq. (9)) and S_{ii}^n is the ASD function of the acceleration measured by *i*-th sensor when there is only TBL background noise (given by Eq. (2)).

The source-induced vibrations and the background noise are not necessarily uniformly distributed over the pipe surface. Hence, the SNR may differ from one sensor to another. For a given location of the monopole source, the most suitable sensor for its detection is the one with the highest SNR. As such, to define the best state at frequency ω, the sensor with the highest SNR is considered as the reference sensor at this frequency. Therefore, the SNR of the reference sensor is provided by,

$$\mathrm{SNR}^{\mathrm{ref}}(\omega) = \max_{i\in[1,n]}[\mathrm{SNR}_i(\omega)]. \tag{13}$$

This state will be considered as a reference to evaluate the increase of the SNR by the beamforming treatment.

The spatial filter of beamforming is characterized by the so-called steering vector $\mathbf{F}_u$, which is defined for each source position *u* in the detection space. For the current problem as described in Fig. 1, the fluid volume in the pipe is taken as the detection space. The beamforming output at position *u*, y_u is given by ([10, 30-33]):

$$y_u(\omega) = \mathbf{F}_u{}^H(\omega)\mathbf{\Gamma}(\omega)\mathbf{F}_u(\omega), \tag{14}$$

where the superscript *H* denotes the Hermitian transpose.

The SNR at the beamforming output is then defined by

$$\mathrm{SNR}^{BF}(\omega) = 10\log_{10}\left(\frac{y_s^s(\omega)}{y_s^n(\omega)}\right) = 10\log_{10}\left(\frac{\mathbf{F}_s{}^H(\omega)\mathbf{\Gamma}^s(\omega)\mathbf{F}_s(\omega)}{\mathbf{F}_s{}^H(\omega)\mathbf{\Gamma}^n(\omega)\mathbf{F}_s(\omega)}\right), \tag{15}$$

where y_s^s and y_s^n are the beamforming steering outputs at the effective source position in the sole presence of the source and in the sole presence of background noise, respectively.

The main advantage of beamforming is that the SNR at the beamforming output is substantially greater than that at the reference sensor. The array gain $G(\omega)$ is obtained from the subtraction [34]

$$G(\omega) = \mathrm{SNR}^{BF}(\omega) - \mathrm{SNR}^{\mathrm{ref}}(\omega). \tag{16}$$

In what concerns the steering vectors, $\mathbf{F}_u$, several definitions have been proposed in literature ([11]) for different applications such as source localisation and detection. In this work, two of them will be considered: (a) that in conventional beamforming as used by Moriot et al. [10], and (b) that in MaxSNR beamforming which focuses on maximizing the SNR at the beamforming output ([11, 29]).

3.2 Conventional beamforming

In this type of beamforming, the transfer functions between the source located at *u* in the detection space and the vibrations measured at *n* sensor positions characterize the wave propagations induced by the source. The transfer functions for a given source position *u* forms the vector $\mathbf{H}_u(\omega) = \left[H_{u,i}(\omega)\right]_{n\times 1}$. The vector component $H_{u,i}(\omega)$ is basically the ratio of the acceleration at the *i*-th sensor to the mass flow acceleration at position *u*. The entries in $\mathbf{H}_u(\omega)$ can be estimated with the numerical model described in section 2.3, as the model allows one to calculate the radial accelerations of the shell when the system is excited by a unit monopole source (i.e., mass flow rate $q_s = 1\ \mathrm{kg\ s^{-2}}$) located at position *u* inside the fluid.

Conventional beamforming assumes that the background noise is spatially homogeneous and incoherent. Therefore, the cross-spectral matrix of accelerations in the sole presence of the background noise can be written as $\mathbf{\Gamma}^n = \sigma\mathbf{I}$, where σ is the ASD function of the acceleration

caused by background noise and **I** is the identity matrix. It can be proved that the beamforming output becomes maximum when it is focused on the effective position of the source and the steering vector is defined by (see [10, 34]),

$$\mathbf{F}_u^{conv}(\omega) = \frac{\mathbf{H}_u(\omega)}{\|\mathbf{H}_u(\omega)\|^2}, \tag{17}$$

where $\|\cdot\|$ represents the Euclidean norm.

Eq. (17) indicates that to compute the steering vector, one needs prior knowledge of the source to estimate the transfer functions $H_{u,i}(\omega)$. In the following, we will suppose that the source is a monopole radiating uniformly in all the direction. As said, it also requires assuming that the background noise is spatially uncorrelated. It is worth noting that conventional beamforming is widely used in many industrial applications for detecting plane wave sources in free space.

3.3 MaxSNR beamforming

As observed by Moriot et al. [10], in some situations involving high flow speeds the measured background noise can be partially correlated. This violates the underlying hypothesis of conventional beamforming and drastically affects its performance.

To overcome this problem, researchers have developed various types of beamforming techniques that essentially rely on the prior knowledge of the background noise and source characteristics [11, 30-32]. In particular, the MaxSNR method was introduced to maximize the SNR at the beamforming output. The optimal steering vector for this beamforming method is given by [11, 30-32],

$$\mathbf{F}_u^{opt}(\omega) = \underset{\mathbf{F}_u}{\operatorname{argmax}} \left[\frac{\mathbf{F}_u{}^H(\omega)\boldsymbol{\Gamma}_u^s(\omega)\mathbf{F}_u(\omega)}{\mathbf{F}_u{}^H(\omega)\boldsymbol{\Gamma}^n(\omega)\mathbf{F}_u(\omega)} \right]. \tag{18}$$

This expression requires knowing the cross-spectral matrices of the background noise $\boldsymbol{\Gamma}^n$ and the leak signal $\boldsymbol{\Gamma}_u^s$ at a given position u. The latter can be obtained as

$$\boldsymbol{\Gamma}_u^s(\omega) = \sigma_s(\omega)\, \bar{\boldsymbol{\Gamma}}_u^s(\omega), \tag{19}$$

where σ_s is the ASD function of the source strength and $\bar{\boldsymbol{\Gamma}}_u^s$ is the normalised CSD function of the signals produced by the source and is given by $\bar{\boldsymbol{\Gamma}}_u^s(\omega) = \mathbf{H}_u(\omega)\mathbf{H}_u{}^H(\omega)$.

Substituting Eq. (19) into Eq. (18) yields the optimal steering vector,

$$\mathbf{F}_u^{opt}(\omega) = \underset{\mathbf{F}_u}{\operatorname{argmax}} \left[\frac{\mathbf{F}_u{}^H(\omega)\mathbf{H}_u(\omega)\mathbf{H}_u{}^H(\omega)\mathbf{F}_u(\omega)}{\mathbf{F}_u{}^H(\omega)\mathbf{\Gamma}^n(\omega)\mathbf{F}_u(\omega)} \right]. \tag{20}$$

The mathematical problem then depends on $\mathbf{\Gamma}^n$ and on $\mathbf{H}_u(\omega)$ through $\bar{\mathbf{\Gamma}}_u^S$. From bilinear algebra considerations ([29-31]), it can be shown that the solution to Eq. (20) is linked with maximizing a ratio of quadratic forms which leads to the generalized eigenvalue problem

$$\bar{\mathbf{\Gamma}}_u^S \mathbf{F}_u^{opt} = \lambda_{max} \mathbf{\Gamma}^n \mathbf{F}_u^{opt}, \tag{21}$$

where λ_{max}, is the largest generalized eigenvalue.

Moreover, as $\bar{\mathbf{\Gamma}}_u^S(\omega) = \mathbf{H}_u(\omega)\mathbf{H}_u{}^H(\omega)$ is a rank-one matrix, corresponding to a single point source, it can be demonstrated that [30, 35]

$$\mathbf{F}_u^{opt} = [\mathbf{\Gamma}^n]^{-1}\mathbf{H}_u. \tag{22}$$

Using the optimized steering vectors $\mathbf{F}_u^{opt}$maximises the SNR at the output of beamforming. Unfortunately, Eq. (22) requires inverting the cross-spectral matrix of the background noise, $\mathbf{\Gamma}^n$, which can be numerically ill-conditioned. To avoid numerical error amplification, and despite $\mathbf{\Gamma}^n$ being a square matrix, we have used the pseudo-inverse algorithm in Matlab to that purpose. That algorithm relies on performing the singular value decomposition (SVD) of the matrix and admits a tolerance threshold so that singular values below tolerance are set to zero. The latter has been chosen as 25 ε max($\mathbf{\Sigma}$), where ε is the machine epsilon (i.e., 2^{-51}) and $\mathbf{\Sigma}$ (for the current case) is a diagonal matrix containing the singular values.

3.4 Broadband frequency analysis

As the water-sodium reaction is a broadband frequency excitation ([6]), it is common practice to perform the beamforming analysis considering all the energy induced by the source in a given frequency band. To that purpose, the time-average of the square signal is estimated after applying a passband filter to it. This can be done by integrating the ASD function over the frequency band $[\omega_1, \omega_2]$. The SNR in the band $[\omega_1, \omega_2]$ for the *i*-th accelerometer reads,

$$\mathrm{SNR}_i[\omega_1, \omega_2] = 10\log_{10}\left(\frac{\int_{\omega_1}^{\omega_2} S_{ii}^S(\omega)d\omega}{\int_{\omega_1}^{\omega_2} S_{ii}^n(\omega)d\omega} \right). \tag{23}$$

The accelerometer with the highest SNR in the band is chosen as the reference sensor, so that

$$\mathrm{SNR}^{\mathrm{ref}}[\omega_1, \omega_2] = \max_{i\in[1,n]}\left[\mathrm{SNR}_i[\omega_1, \omega_2]\right]. \quad (24)$$

Finally, to calculate the beamforming output level for the frequency band, one can numerically evaluate the integral of the output $y_u(\omega)$ between ω_1 and ω_2. In this way, we get the SNR at the output and the array gain for a whole frequency band instead of for a single frequency.

4. Analysis of the array signals induced by the monopole source and by the turbulent flow

4.1 Vibration characteristics of the test section

Before analysing the beamforming performances, it is worth reminding some dynamic characteristics of the modelling of the SGU system in [1]. More details can be found in [12].

The forces exerted by the stiffeners as well as by the internal fluid excite the cylindrical shell in the radial direction. To account for the waves propagating in the axial direction in reaction to these radial forces, we estimate the spectrum of the shell radial displacements for a unit spectral force (i.e., taking $\tilde{\tilde{F}}(k_x, n) = 1$ in Eq. (4)). This is analogous to considering the shell is excited by a point force of amplitude 2π at $(0,0)$. Fig. 3 presents a colormap of the displacements' dependence on frequency and on the axial wavelength $\lambda_x = 2\pi/k_x$, for the circumferential orders *n*=2 and *n*=3. The trajectories observed in the figure can be attributed to dispersion curves and reveal the presence of propagative waves. In fact, it should be noted that these curves depend on the excitation and that they are different from classical dispersion curves, which are usually found from the roots of the denominator $\tilde{\tilde{\Delta}}$ of Eq. (4). The shell sensitivity to the excitation can be inferred from the levels of the trajectories. It becomes apparent from the figure that the shell strongly reacts above the cut-on frequencies of the circumferential orders *n*=2 and *n*=3, which have respective values 360 Hz and 1072 Hz. The axial wavelength associated to these propagative waves decrease strongly just above the cut-on frequency and this reduction becomes less important as the frequency increases. When the fluid filled shell gets coupled to the ring stiffeners, the propagating waves partially reflect at the interface between the stiffener and the shell (due to the mechanical impedance mismatch). The interferences between the reflected waves and the outward propagating ones result in resonances at some frequencies. We call the latter pseudo axial modes as they correspond to axial standing waves generated from partial wave reflection at the stiffeners. To extract these resonant frequencies, the radial displacements of the fluid filled shell coupled to the ring

stiffeners have been calculated under a unit radial force excitation applied in an arbitrary point between the two ring stiffeners. From the frequency peaks in the resulting spectra (not shown herein), one can identify the resonant frequencies of the pseudo axial modes for n=2 and n=3 presented in Table 1. One observes that the frequency spacing between two consecutive modes (for a given circumferential order) increases when the axial modal order, m, augments. This is a direct consequence of the shape of the trajectories in Fig. 3. It is known that the standing waves (pseudo axial modes) exhibit nodes of vibration spaced by half a wavelength. The resonances thus occur approximately when the propagative wavelength is a subdivision of twice the distance between the two stiffeners. As the propagative wavelength decreases strongly after the cut-on frequency, many frequencies just beyond the cut-on satisfy such rule. In other words, several pseudo axial modes emerge once past the cut-on frequency (see Table 1). For the highest frequencies, however, the axial wavelength diminishes more slowly. Consequently, the spacing between consecutive frequencies fulfilling the rule increases and so does the spacing between pseudo axial modes.

On the other hand, and as remarked in [12], the shell response under radial excitation for the circumferential order n=0 is very small compared to that for other orders. Moreover, for n=1 pseudo axial waves do not manifest because the shell is more rigid than the stiffener. In this case, almost no reflection occurs as the propagative waves hardly notice the presence of the stiffeners. Consequently, we will not analyse the model for circumferential orders n=0 and n=1 as they do not play a major role for the present study.

Table 1. Frequencies of the pseudo axial modes *(m,n)* for the circumferential order, $n \in \{2,3\}$ and the axial order, $m \in \{1 \ldots,10\}$.

m	1	2	3	4	5	6	7	8	9	10
n=2 / $f_{(2,m)}$ (Hz)	360	372	400	456	544	659	799	955	1125	1304
n=3 / $f_{(3,m)}$ (Hz)	1072	1077	1086	1102	1125	1158	1201	1256	1324	1411

4.2 Vibrations induced by the turbulent boundary layer

Next, let us focus on the signals measured by the accelerometer array when the system is solely excited by the TBL. For the assessment of the beamforming performance, the TBL will be considered as the origin of the background noise between the array sensors. The calculations have been carried out following the numerical process described in section 2.2. Fig. 4a shows

the distributions of the ASD of the acceleration in terms of the accelerometer number and frequency for a flow rate of 140 l s^{-1}. The frequencies of the pseudo axial modes for n=2 and n=3 have been marked by horizontal dash and dash-dotted lines, respectively. Their influence is clearly confirmed. The pattern in Fig. 4a at the resonance frequencies shows some bumps and nodes. The distances between two nodes are associated with half the wavelength of the propagative waves, as commented for Fig. 3. For example, at 659 Hz and 955 Hz these distances are respectively 0.48 m and 0.36 m. The corresponding wavelengths for these two distinct frequencies are 0.98 m and 0.74 m, as shown in Fig. 3a.

The normalized CSD of the radial acceleration between all accelerometers and accelerometer #12 is plotted in Fig. 4b as function of frequency. Even though the TBL excitation is almost spatially uncorrelated, a considerable spatial correlation in the vibration field of the shell is observed over the entire frequency range. This aspect was addressed in detail in [12]. The red patterns in Fig. 4b correspond to strong coherence regions clearly related to the pseudo axial modes.

4.3 Signals induced by the monopole source to be detected

In this section, we turn our attention on the signals measured by the accelerometer array when the system is excited by the monopole source to be detected. The calculations are performed as described in section 2.3. Hereafter and to shorten notation, a point with cylindrical coordinates (x,π,r) will be simply designated as (x,-r). Fig. 5 shows the distributions of the ASD of the acceleration as a function of the accelerometer number and frequency for two radial positions of the source: $r_s = 0.09$ m corresponding to a position close to the array and $r_s = -0.03$ m, which is near the centre of the pipe. For both cases, the axial position is $x_s = 0.6$ m that corresponds approximately to the middle of the sensor array length. The frequencies of the pseudo axial modes for n=2 and n=3 have also been marked in Fig. 5. The mass flow acceleration amplitude of the oscillating source has been fixed to 10^{-4} kg s^{-2} at all frequencies to have a SNR on the reference sensor of ~ 0 dB in the middle of the frequency band of interest.

One can notice from the figure that, generally, the levels are significantly greater when the source is close to the array (i.e., for $r_s = 0.09$ m in Fig. 5a). This can be explained by the divergence of the spherical waves produced by the monopole and because, as explained below, only the components of the blocked pressure of the source corresponding to the first circumferential orders n=0 and n=1 are significant for a source position close to the centre of the pipe. In such case, the patterns in Fig. 5b present some similarities with those in Fig. 4a for

some frequencies (e.g., between 200 Hz and 500 Hz and between 700 Hz and 1100 Hz). For other frequency bands, the patterns are clearly different for the two source positions as well as for the TBL excitation. This can be understood by the fact that the monopole source does not excite the same pseudo axial modes than the TBL (see Fig. 3). In addition, the radial position of the source also influences them. For instance, for a source located on the shell axis (i.e., r_s =0 m), only the circumferential order n=0 would be excited because the problem becomes fully axisymmetric. As the source moves away from the shell centre, more circumferential orders contribute to the shell response. This explains why the red patterns are more complex for $r_s = 0.09$ m in Fig. 5a than for $r_s = -0.03$ m in Fig. 5b. For frequencies beyond 1200 Hz, the circumferential order n=2 gets more excited for the source at $r_s = 0.09$ m than at $r_s = -0.03$ m. Finally, it should be emphasized that as the acoustic monopole is a deterministic excitation, the normalized CSD of the radial acceleration between the different sensors is strictly equal to one regardless of frequency.

5. Analysis of the beamforming performance

So far, we have separately analysed the accelerometer signals induced by the leak (represented by a monopole) and by the background noise (represented by the TBL). These signals can be used to compute the steering vectors and to assess the performance of beamforming techniques following the developments in section 3. In what follows, we will perform narrow and broadband beamforming analysis for the leakage problem at hand.

5.1 Narrow band analysis

Fig. 6 presents the reference sensor and the reference SNR as a function of frequency for the acoustic source located near the array, $(x_s, r_s) = (0.06\text{ m}, 0.09\text{ m})$, and a flow rate of 140 l s^{-1}. One can notice that the reference sensor varies from one frequency to another in the considered frequency band [200 - 2000] Hz. This is because the spatial distribution of the vibratory field induced by the turbulent flow (see Fig. 4) and by the source (see Fig. 5) is frequency dependent. The SNR of the reference sensor shows an upward trend with frequency. This is mainly due to the downward drift of the background noise and a slight increase in the source signal over frequency. Moreover, the frequencies of local minima in Fig. 6 correspond to the pseudo-axial modes.

The beamforming outputs for the acoustic source and for the background noise have been individually estimated from Eq. (14) with $\mathbf{\Gamma} = \mathbf{\Gamma}^s$ and $\mathbf{\Gamma} = \mathbf{\Gamma}^n$, respectively. These quantities

have been obtained for the beamforming focusing on the source. Furthermore, the steering vectors have been respectively computed from Eqs. (17) and (18) for the conventional and MaxSNR beamforming techniques, with u=s standing for the source position. One can then estimate the SNR at the beamforming output using Eq. (15). Its values for the two beamforming methods are compared to the SNR of the reference sensor in Fig. 7. As observed, the SNR of the conventional beamforming (Class. BF in the figure) is close to that of the reference sensor, while that of the MaxSNR is about 20 dB higher. The conventional beamforming results exhibit local minima at the resonant frequencies whereas the MaxSNR ones show a monotonic trend.

The difference between the SNR at the beamforming output and the SNR of the reference sensor provides the array gain as defined by Eq. (16). That quantifies the quality of the beamforming technique. The computed array gains are shown in Fig. 8 for the two source positions tested in section 4.3, namely $(x_s, r_s) = (0.6, 0.09)$ m (studied in Figs. 6 and 7) and $(x_s, r_s) = (0.6, -0.03)$ m. For the two source positions, the gain of the MaxSNR beamforming is substantially greater than that of the conventional beamforming over the entire frequency range. This is because the steering vectors of the MaxSNR method are formulated such that they provide maximum SNR at the beamforming output, whilst assuming an uncorrelated background noise in the conventional beamforming is not valid for the current problem. Although, the gain of the conventional beamforming is relatively low (sometimes even negative), it can reach some moderate values (i.e., 6-8 dB) at certain frequencies between resonant frequencies. As said, this poor performance can be attributed to the strong coherence of the vibratory field induced by the TBL. That was observed in Fig. 4b for those frequencies corresponding to the pseudo axial modes. To confirm this hypothesis, we have calculated the gain of the conventional beamforming using a homogeneous uncorrelated background noise (as the one induced that the electronic perturbations) instead of using the TBL one. The result is depicted in Fig. 8 (red dotted line with the legend "Theory"). A substantial improvement is achieved, the new SNR fluctuating around 11 dB and being always greater than that obtained with the TBL background noise. This confirms that the background noise coherence adversely affects conventional beamforming at the pseudo axial modes' frequencies. In contrast, the MaxSNR beamforming presents significant gains (always greater than 10 dB) and local maxima are observed at resonances. This is because the SNR at the MaxSNR beamforming output does not depend strongly on the resonant frequencies, as shown in Fig. 7, whereas the SNR of the reference sensor and conventional beamforming present local minima for them. On the other

hand, it can be observed in Fig. 8 that the array gain is greater for the source position close to the pipe centre than for the source in the array vicinity.

For better understanding why the MaxSNR beamforming exhibits superior performance to conventional beamforming, the separate cross-spectral matrices of the vibration signals induced by the monopole point source to be detected and by the TBL background noise at 700 Hz are plotted in Fig. 9. Before the analysis of that figure, it should be emphasized that the beamforming performance cannot be determined by directly comparing the highest values of the elements of the source and the background noise cross-spectral matrices. The reason is that to define the SNR of the reference sensor, the values of the diagonal terms of the matrices that correspond to the ASD of the acceleration are used. The array gain is defined by comparing the SNR of the beamforming output with the SNR of the reference sensor, which makes it mostly independent of the highest values of the elements of the cross-spectral matrices. The superior performance of the MaxSNR beamforming is therefore linked to the pattern difference between the cross-spectral matrix of the background noise, which should be minimized, and that of the source, which should be enhanced. Fig. 9a shows the cross-spectral matrix corresponding to the TBL while Figs. 9b-c show those for the source located at $(x_s, r_s) = (0.6, 0.09)$ m and $(x_s, r_s) = (0.6, -0.03)$ m, respectively. The TBL magnitude pattern in Fig. 9a (first row) is similar to that of the source at $(x_s, r_s,) = (0.6, 0.09)$ m in Fig. 9b. However, the patterns for the phase (second row in the figure) are very different, indicating that the pipe vibrations have been produced by two different types of sources. The TBL is a stochastic excitation that induces a wall pressure field with a uniform spatial distribution. As a result, the phase is either 0 or 180° (see Fig. 9a). On the contrary, the acoustic source is a deterministic excitation that is spatially localised and induces a wall pressure field that results from the acoustic wave propagation inside the pipe. Therefore, the phase variations are related to the different wave travelling times from the source to the different sensor positions (see Fig. 9b). In the case of the source located close to the pipe centre (see Fig. 9c), the differences become more apparent and even the patterns of the amplitudes are significantly different from those of the TBL. The different acoustic wave travelling times between the source and the pipe wall play a more important role. That is inexistent for the TBL, which directly excites the pipe. These dissimilarities between the amplitudes and phases of the cross-spectral matrices of the source and those of the background noise explain why the MaxSNR beamforming performs better than the conventional one. The acoustic source and TBL excitations are very different in nature and the

MaxSNR beamforming can dissociate them, enhancing the source signal while cancelling the background noise one.

5.2 Broadband analysis

In what follows, we will consider broadband beamforming analysis as it is of interest for the practical application at hand. Also, the influence of some parameters on the beamforming performance will be investigated.

5.2.1 Nominal case

We consider frequency bands $[\omega_1, \omega_2]$ being 200 Hz in bandwidth and comprising the range from 200 Hz to 2000 Hz. Fig. 10 shows the reference sensor for each band and its corresponding SNR. The SNR of an accelerometer for a given frequency band is defined by Eq. (23) and the reference sensor for the band is chosen from Eq. (24). Here, we address the same situation of section 5.1, but using a broadband analysis. The comparison between Fig. 10 and Fig. 6 reveals that the SNRs of the reference sensor for the narrow band analysis reach higher values than the broadband ones. This is because the reference sensor changes for each frequency in a band when performing a narrow band analysis, while a single reference is assigned to all frequencies in the band, in the broadband case.

Fig. 11 plots the array gain of each band for the two source locations and using both, the conventional and MaxSNR beamforming approaches. As for the narrow band case, the array gain of the MaxSNR beamforming is very significant and it varies between 18 dB and 28 dB for the source at $(x_s, r_s) = (0.6, 0.09)$ m and between 28 dB and 42 dB for the source at $(x_s, r_s) = (0.6, -0.03)$ m. In fact, these values appear generally greater than those obtained in the narrow band analysis. This may be because different pre-filtering references were applied in the two analyses and because of integrating the beamforming output over the frequency bandwidth. The MaxSNR beamforming clearly outperforms again the conventional one. Given that, only results for the MaxSNR method will be presented in the remaining of this work.

In Fig. 12, we can observe how the MaxSNR gain varies as a function of the source position, for the frequency bands [400 – 600] Hz and [1800 – 2000] Hz. The detection space in the plane $\theta = 0$ has been discretized with a rectangular and regular grid of points. The axial coordinates of these points vary between 0.2 m and 2.8 m with a step size of 0.2 m, while the radial coordinates comprise from -0.09 m to 0.09 m with a step size of 0.15 m. The array is located between the axial positions x_1 =0.15 m and x_{25} =1.11 m, as represented by the

horizontal black line in the *x*-axes of Fig. 12. The gain exhibits a strong dependence with the source position in the detection space. Two different general tendencies can be observed: (a) for a given axial position, the gain looks greater for the source close to the centre of the pipe than near the shell wall; (b) for a given radial position, the gain is mostly superior for the axial positions in front of the array. Yet, it remains significant far away from it. This implies that the MaxSNR beamforming can be efficient even if the source is not in front of the array, and in particular, if it is close to the pipe's central axis (small radial coordinate).

Fig. 13 presents the maximum acceleration measured by the array as a function of the source position in the detection space, for the two frequency bands already considered in Fig. 12. One can appreciate that the acceleration is much smaller when the source is closer to the pipe centre than to the shell wall. The reason for that is twofold: (a) the spherical divergence of the wave generated by the monopole source; (b) basically the components of the shell displacements corresponding to the first circumferential orders, n=0 and n=1 get excited when the source is near the pipe axis. The first phenomenon appears to be less important as the maximum acceleration seems not to meaningfully depend on the source axial position. As regards the second phenomenon, the analysis of the operational dispersion curves for a radial force excitation in section 4.1 has already revealed that the response of the shell is less significant for n=0 and n=1 than for n=2 and n=3, in the considered frequency band [200 2000] Hz. When the source approaches the centre of the pipe, only the low responding circumferential orders n=0 and n=1 get significantly excited, whereas the orders n=2 and n=3 get triggered when approaching the shell wall. From Figs. 12 and 13, one can deduce that the maximum array gain is attained when the measured maximum acceleration is minimum. This is of practical interest because when the maximum acceleration induced by the source is low, the SNR of the reference sensor is also low. Therefore, detecting the source with a threshold criterion may be difficult if one only considers the reference sensor. Yet, if the array gain is high, the SNR of the beamforming output significantly increases, which eases source detection.

For completeness, in Fig. 14 we show the array gain in the detection space for $\theta = 90°$, i.e., at a normal plane with respect to that in Fig. 12. As in Fig.12, the gain is high for the source positions close to the pipe centre. When getting closer to the shell, the gain values resemble those in the detection space $\theta = 0°$ for the source positions opposite to the array location (i.e., for $r_s \leq -0.7$ m).

5.2.2 Influence of damping and flow velocity

The models developed in this work allow one to study the influence of different physical and geometrical parameters on the MaxSNR beamforming performance. In this section, we limit our investigation to the effects of damping and flow rate. The former is difficult to estimate accurately in practice whereas the latter can vary during the different operational states of a steam generator unit. Therefore, a sensitivity analysis of these parameters would provide useful practical insight.

It should be noted that for the nominal case above, the value of the damping loss factor was chosen to be 0.1 % for both shell and water. The array gains using a damping loss factor of 1% are now plotted in Fig. 15. As observed, the gains remain significant though they decrease about 8-10 dB. The spatial distribution of the gains is, however, very similar to that in Fig. 12 for a loss factor of 0.1 %. A narrow band analysis (not shown herein) revealed that the sensors' accelerations depend on damping. The variations are only meaningful for frequencies close to the resonant ones for the monopole excitation, but they affect the entire frequency range for the TBL excitation. Hence, the reference sensor needs not necessarily to be the same for different damping values. It was checked that the SNR of the reference sensor for the 1% damped case was from 6 to 11 dB higher than that of the nominal case (depending on the frequency band). As opposed, the beamforming output is not very sensitive to changes in damping regardless of the excitation type. In summary, the SNR at the beamforming output is basically insensitive to damping variations, whereas that of the reference sensor increases with damping. This results in a decrease of the array gain when augmenting the damping value. On the other hand, one could wonder whether the gain is controlled by the damping of the steel shell or by that of the water. To answer this question, supplementary simulations were carried out. Results showed that the gain is mainly independent of the variation of the fluid damping. Very similar results to those in Fig. 15 were obtained by setting the shell damping to 1% and that of the water to 0.1%.

To analyse the influence of the flow rate on the MaxSNR beamforming performance, we consider a flow rate of 560 l s^{-1} (i.e., four times the nominal flow rate in the previous subsection). Under that circumstance, the SNR of the reference sensor showed a decrease of 36 dB, which is consistent with the law for hydrodynamic noise level (that grows with the velocity to the power of 6). In contrast, the array gain was not substantially affected. A difference of less than 0.5 dB was obtained when comparing to the nominal case (the results have not been plotted here for the sake of brevity). This can be explained by the fact that the frequency of interest is

well above the hydrodynamic coincidence, which is 0.04 Hz and 0.6 Hz for a flow rate of 140 l s^{-1} and 560 l s^{-1}, respectively. Therefore, only the low wavenumber of the sub-convective domain in the wall pressure field induced by the TBL plays an important role [22]. The shape of the wavenumber spectrum is relatively flat in the low wavenumber domain and independent of flow speed. Consequently, the nature of the excitation does not substantially vary when changing the flow rate. Only the overall level of the wall pressure field increases. This explains why the SNR of the reference sensor has changed but not the array gain.

5.3 MaxSNR beamforming output in the detection space

To end this study, the beamforming output levels in the detection space $\theta = 0°$ for the nominal situation were studied for four different cases in the frequency bands [400 – 600] Hz (Fig. 16) and [1800 – 2000] Hz (Fig. 17). In Case 1, there is no monopole source and the pipe is only excited by the TBL. In Case 2, the pipe is excited by the TBL (background noise) and by a monopole source placed near the shell wall. The monopole is located close to the pipe centre in Case 3. Finally, in Case 4 we consider a scenario in which the source is far from the accelerometer array. The results in Figs. 16 and 17 have been obtained by controlling the source strength such that the SNR for the reference sensor equals zero for each source position. Moreover, the dynamic ranges of the levels in each figure have been kept identical to facilitate the comparison of the considered cases with and without the source.

Fig. 16a shows the output levels only produced by the background noise (i.e., without the source to be detected). Those are close to 27 dB everywhere except for a light blue spot in front of the array that reaches 31 dB. The output levels in the presence of the monopole source are shown in Figs. 16b-d for the three source positions of Cases 2 to 4. The real location of the source is indicated with a white cross. One notices that the highest level of output in the detection space occurs at the real location of the source in Fig. 17b, but this is not the case in Figs. 16c and 16d. For the latter, the output level distribution is mostly uniform in the detection space. In this sense, we should remark that the main advantage of MaxSNR beamforming with respect to conventional beamforming is to improve the SNR for source detection, but the technique is not as efficient for source localization. In Fig. 16c, the map of the beamforming output does not allow us to localize the real position of the source. However, comparing the map in Fig. 16a (without source) with that in Fig. 16c (with source) it becomes possible to detect the source despite the SNR of the reference sensor being zero. This clearly highlights the effectiveness of the MaxSNR beamforming technique. Fig. 16c also shows that the output level increases more than 40 dB in the most part of the detection space and it increases 42.5 dB at the source position,

which corresponds to the array gain. For Case 4, where the source is away from the array position, the increase of the output level is not as strong as for Case 3, but it still remains significant (around 25-29 dB). This is consistent with the fact that this configuration corresponds to an array gain of 29.1 dB. The relatively poor performance of the MaxSNR beamforming for this case can be compensated, however, by the fact that for this position the source can induce substantial array signals as shown in Fig. 13. This cannot be highlighted in Fig. 16, though, because the SNR on the reference sensor has been forced to zero dB.

Fig. 17 presents similar analyses to those in Fig. 16 for the band [1800 2000] Hz. The above-mentioned discussion and observations are essentially valid for this figure, yet some differences manifest. Although the spatially uniform TBL completely excites the cylindrical shell, the beamforming output levels are not uniform in the detection space. This is mainly attributed to the ring stiffeners, which lead to a non-uniform distribution of the shell vibrations. Whilst the array gains for this band are lower than that of the previous considered band, the maps of the output beamforming still allow us to identify the presence of the source. The most difficult scenario is when the source is far away from the array and the gain is limited to 12.3 dB. It should be stressed that even though the MaxSNR beamforming output does not reach a maximum at the real source location (see Figs. 17c and 17d), the detection of the source with a threshold criterion is possible because the array gain is still significant.

6. Conclusions

Numerical models of a fluid-filled pipe coupled to two ring stiffeners and excited by an acoustic monopole source and/or a TBL have been developed to assess the array gain of the conventional and MaxSNR beamforming techniques, in the case of an accelerometer array mounted on the pipe surface. The investigations on the beamforming performance have been carried out on a configuration mimicking the experimental set-up considered in [1]. However, the proposed numerical methodology can be of interest to more general problems of acoustic source detection in pipes with a noisy, turbulent background excitation (for instance, for a pipe filled with oil and with periodically space stiffeners). The introduced numerical modelling permits to easily control all the system parameters and to carry out a deep analysis of the beamforming outputs. Although the proposed method has been used herein for source detection, it could be implemented as well for localization purposes in some industrial applications. The proposed methodology has proved to be a good complement for better understanding the results from experimental mock-ups or in-situ tests.

It has been shown that the conventional beamforming exhibits low, or even negative, array gain at the frequencies of the pseudo axial modes. Strong coherences of the flow-induced vibrations of the pipe at these frequencies are responsible for the poor performance of conventional beamforming, which relies on assuming an uncorrelated background noise. For frequencies between resonances, the spatial coherence of the flow-induced vibration field is weaker, and the array gain can reach some moderate values (from 5 dB to 10 dB). However, the gain for broadbands is penalised by the low values of the gain at the resonant frequencies.

On the other hand, the MaxSNR beamforming technique has shown significant array gains, both for narrow and broadband analyses. It has been observed that the beamforming output is not sensitive to the presence of the pseudo axial modes. Furthermore, the SNR of the reference sensor generally presents local minima at resonances, while the gain reaches local maxima at these frequencies. It has been also found that the gain is higher for the source positions close to the centre of the pipe than for those near the pipe wall, while the opposite occurs for the signal amplitudes. The beamforming can then compensate the weakness of the signals for detecting sources near the centre of the pipe. The gain remains also significant for source positions which are not in front of the array. Moreover, the flow speed shows little influence on the gain for the considered frequencies, which are well above the hydrodynamic coincidence frequency. It has been also demonstrated that the higher the damping of the pipe is, the lower are the gain values in the broadband analysis.

Finally, it has been demonstrated that the MaxSNR beamforming technique is not well adapted for source localisation in the considered system because the output does not necessarily become maximum at the source position. However, the MaxSNR beamforming enhances the signal induced by the source while it cancels that produced by the turbulent flow. A significant increase of the beamforming output in the detection space is observed in the presence of the source, which facilitates its detection using a threshold criterion. In the context of sodium leaks in the SGU of a liquid SFR, the early detection is important since sodium/water reactions can lead to critical damage if appropriate action is not taken immediately. The ability of the beamforming method to improve the SNR is then of prime importance to help detecting the presence of the water-sodium reaction when the leak is small (i.e., lower than 1 g/s). If a leak is detected, the process for preserving the SGU should be urgently activated. However, the localization of the leak in the SGU can be done in a second step to get supplementary information to help solving the problem. Investigations on the laboratory mock-up have shown that the MaxSNR beamforming approach can be very efficient to quickly detect the source,

even when the signals induced by the source are smeared by the background noise. However, before to deploy this technique in a SFR context, these results deserve to be confirmed in the future on more realistic prototypes of an SGU, than the mock-up considered so far.

Acknowledgments

This work was carried out in the framework of the LabEx CeLyA ("Centre Lyonnais d'Acoustique", ANR-10-LABX-60) and the Sodium Technology project of GEN4 program (R4G/TECNA) of the IRESNE Institute (Research Institute for Nuclear Systems for Low Carbon Energy Production) of CEA.

References

[1] Kassab, S., Michel, F., Maxit, L., Water experiment for assessing the vibroacoustic beamforming gain in the framework of the acoustic leak detection for the sodium-heated steam generator, Mech. Syst. Signal Process. 134 (2019) 106332.

[2] Guépié, B.K., Grall-Maës, E., Beauseroy, P., Nikiforov, I., Michel, F., Reliable leak detection in a heat exchanger of a sodium-cooled fast reactor, Ann. Nucl. Energy 142 (2020) 107357.

[3] Cavaro, M., Payan, C., Jeannot, J.P., Towards the bubble presence characterization within the SFR liquid sodium, In: Proceedings of ANIMMA International Conference, Marseille, France, vol. 1127, June 2013.

[4] Chikazawa, Y., Acoustic leak detection system for sodium-cooled reactorsteam generators using delay-and-sum beamformer. J. Nucl. Sci. Technol. 47(1) (2010) 103–110.

[5] Hayashi, K., Shinohara, Y., Watanabe, K., Acoustic detection of in-sodium water leaks using twice squaring method. Ann. Nucl. Energy 23 (1996) 1249-1259.

[6] Kim, T., Yugay, V. S., Jeong, J., Kim, J., Kim, B., Lee, T., Lee, Y., Kim, Y., Hahn D., Acoustic Leak Detection Technology for Water/Steam Small Leaks and Microleaks Into Sodium to Protect an SFR Steam Generator. Nucl. Technol. 170 (2010) 360-369.

[7] Chikazawa, Y., Yoshiuji, T., Water experiment on phased array acoustic leak detection system for sodium-heated steam generator. Nucl. Eng. Des. 289 (2015) 1-7.

[8] Moriot, J., Passive vibroacoustic detection of a water-sodium reaction using beamforming on a steam generator of a liquid sodium fast reactor, PhD thesis, INSA Lyon, France, 158 p. (in French), 2013.

[9] Moriot, J., Maxit, L., Guyader, J.L., Detection and localization of a leak in a sodium fact reactor steam generator by vibration measurements. In: Proceedings of Euronoise, Prague, Czech Republic, June 2012.

[10] Moriot, J., Maxit, L., Guyader, J.L., Gastaldi, O., Périsse, J., Use of beamforming for detecting an acoustic source inside a cylindrical shell filled with a heavy fluid. Mech. Syst. Signal Process. 52–53 (2015) 645–662.

[11] Van Veen, B., Buckley, K., Beamforming: a versatile approach to spatial filtering. IEEE ASSP magazine 5 (2), (1988) 4-24.

[12] Maxit L, Karimi M., Guasch O., Spatial coherence of pipe vibrations induced by an internal turbulent flow, J. Sound Vib. 493 (2021) 115841.

[13] Bonness, W., Capone, D., Hambric, S., Low-wavenumber turbulent boundary layer wall-pressure measurements from vibration data on a cylinder in pipe flow, J. Sound Vib.329 (2010) 4166-4180.

[14] Leissa A.W., Vibration of shells. Washington: Scientific and Technical Information Office, National Aeronautics and Space Administration, USA, 1973.

[15] Junger M.C., Feit D., Sound, structures, and their interaction, Second edition, MIT Press, 1986.

[16] Tran-Van-Nhieu, M., Scattering from a ribbed finite cylindrical shell. J. Acoust. Soc. Am. 10 (2001), 2858–2866

[17] Flinovia – Flow induced noise and vibrations issues and aspects: A focus on measurement, modeling, simulation and reproduction of the flow excitation and flow induced response. Springer International Publishing Switzerland, 2015, pp. 357.

[18] Chase, D.M., The character of the turbulent wall pressure spectrum at subconvective wavenumbers and a suggested comprehensive model, J. Sound Vib. 112 (1987) 125-147.

[19] Graham W.R., A comparison of models for the wavenumber-frequency spectrum of turbulent boundary layer pressures, J. Sound Vib. 206 (1997) 541-565.

[20] Williams E.G., Fourier Acoustics: Sound Radiation and Nearfield Acoustical Holography, Academic Press, London UK, 1999.

[21] Photiadis D.M., Williams E.G., Houston B.H., Wave-number space response of a near periodically ribbed shell, J. Acoust. Soc. Am. 101, (1997) 877-886.

[22] Maxit L., Karimi M., Meyer V., Kessissoglou N., Vibroacoustic responses of a heavy fluid loaded cylindrical shell excited by a turbulent boundary layer, J. Fluids Struct. 92 (2020) 102758.

[23] Maury C., Gardonio P., Elliott S.J., A wavenumber approach to modelling the response of a randomly excited panel. Part I: general theory, J. Sound Vib. 252 (2002) 83–113.
[24] Maxit, L., Denis, V., Prediction of flow induced sound and vibration of periodically stiffened plate, J. Acoust. Soc. Am. 133 (2013) 146-160.
[25] Fahy F., Sound and Structural Vibration: Radiation, transmission and response, Academic Press, Orlando, USA, 1985. 325 p.
[26] Maxit L., Ginoux J.M., Prediction of the vibroacoustic behavior of a submerged shell non periodically stiffened by internal frames, J. Acoust. Soc. Am. 128 (2010) 137-151.
[27] Fuller C.R., Fahy F.J., Characteristics of wave propagation and energy distributions in cylindrical elastic shells filled with fluid. J. Sound Vib. 81 (1982) 501–518.
[28] Fuller C.R., Monopole excitation of vibrations in an infinite cylindrical elastic shell filled with fluid, J.SoundVib. 96 (1984) 101–110.
[29] Tanaka, T., Shiono, M., Acoustic Beamforming with Maximum SNR Criterion and Efficient Generalized Eigenvector Tracking. In: Proceeding of the 15th Pacific-Rim Conference on Advances in Multimedia Information Processing, Malaysia, December 2014.
[30] Van Trees H.L., Optimum Array Processing. Part IV of Detection, Estimation and Modulation Theory, John Wiley & Sons, Inc., New York, USA, 2002.
[31] Monzingo R.A., Haupt R.L, Miller T.W., Introduction to Adaptive Arrays, Scitech, Raleigh, USA, 2011.
[32] Manolakis D.G., Ingle V.K., Kogon S.M., Statistical and Adaptive Signal Processing: Spectral Estimation, Signal Modeling, Adaptive Filtering and Array Processing, Artech House, Norwood, USA, 2005.
[33] Johnson D.H, Dudgeon D.E, Array signal processing: concepts and techniques. Prentice Hall, Houston, USA, 1993.
[34] Brandstein M., Ward D., Microphone Arrays: Signal Processing Technique and Applications. Springer, New York, USA, 2001.
[35] Warnick K. F., Jensen M. A., Antennas and propagation for wireless communications, ECEn 665. Chapter 13: adaptive beamforming, Lecture Notes, Brigham Young University, Provo, USA, April 2015.

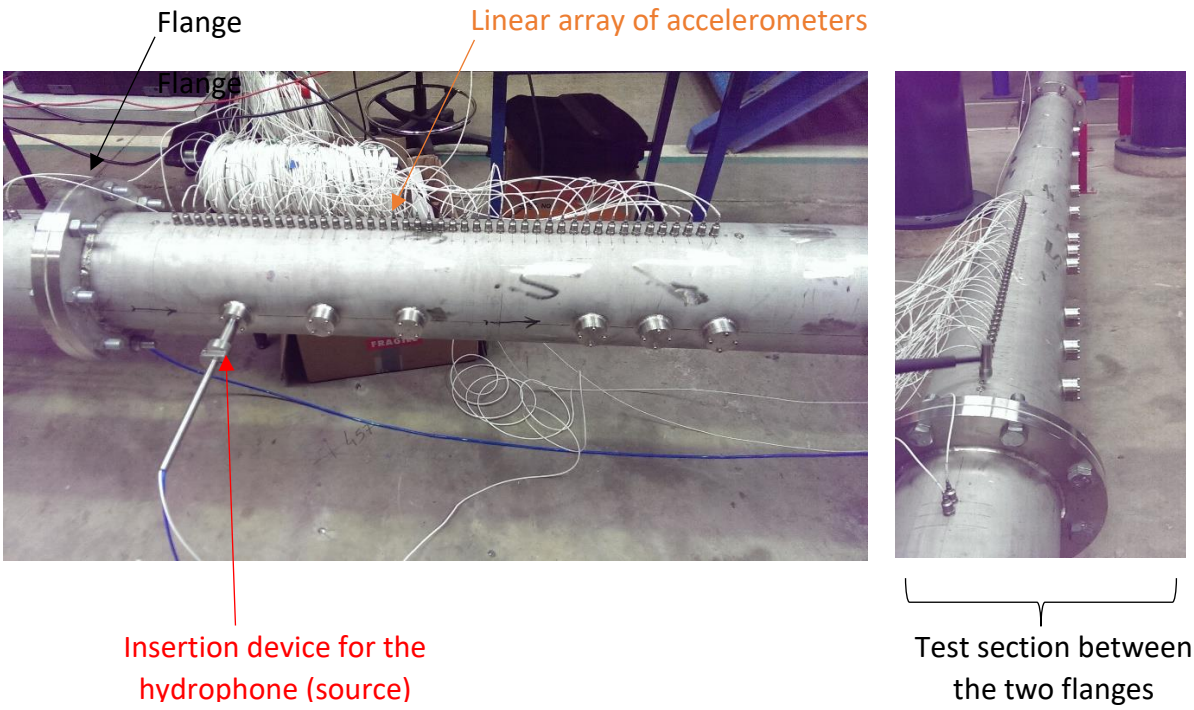

(a)

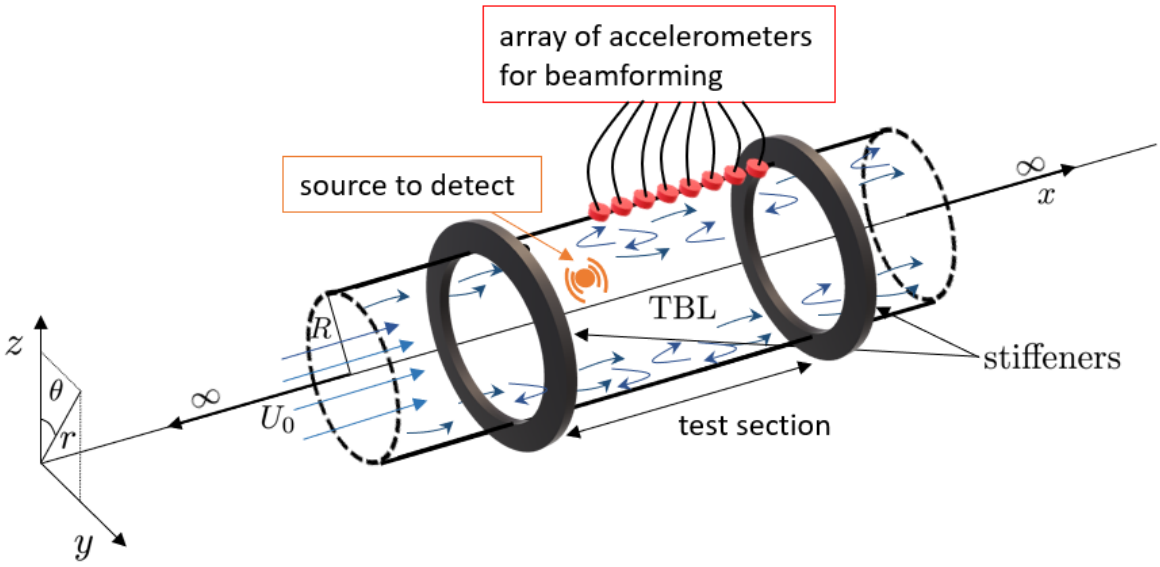

(b)

Figure 1. (a), experimental set-up considered in [1]; (b), schematic representation of the model configuration employed for assessing the performance of the vibroacoustic beamforming.

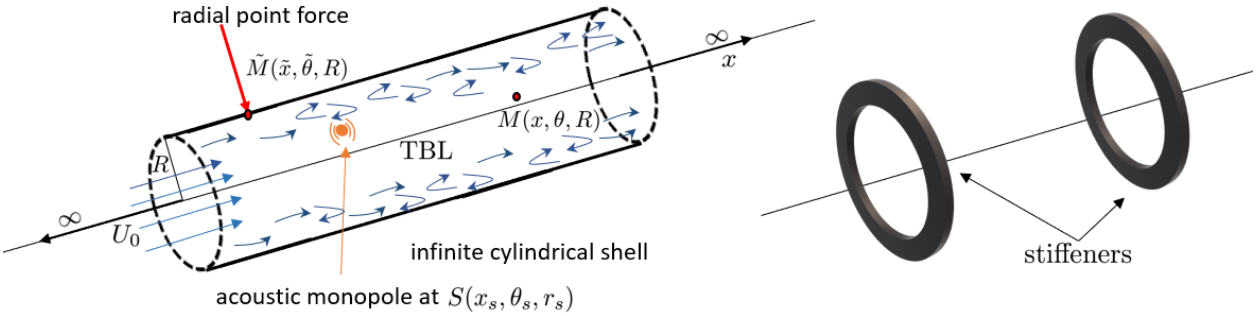

(a) (b)

Figure 2. Partitioning of the vibroacoustic problem for the circumferential admittance approach: (a), fluid filled cylindrical shell; (b), ring stiffeners.

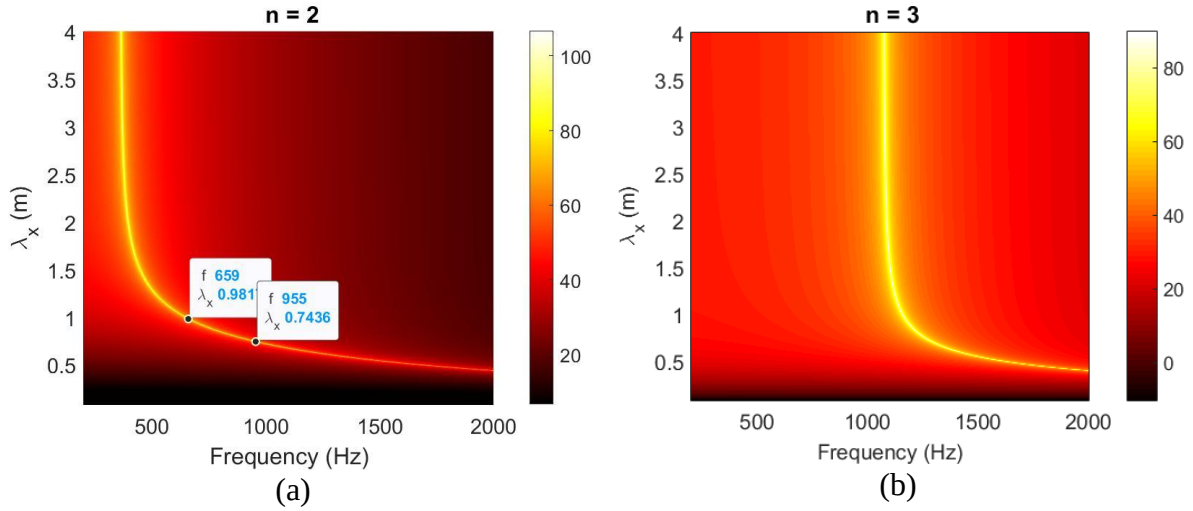

Figure 3. Level (dB, ref. 1 $m^2.N^{-1}$) of the spectral displacement of the fluid filled shell under a radial point force excitation as a function of frequency and axial wavelength $\lambda_x = 2\pi/k_x$ for (a) n=2 (b) n=3.

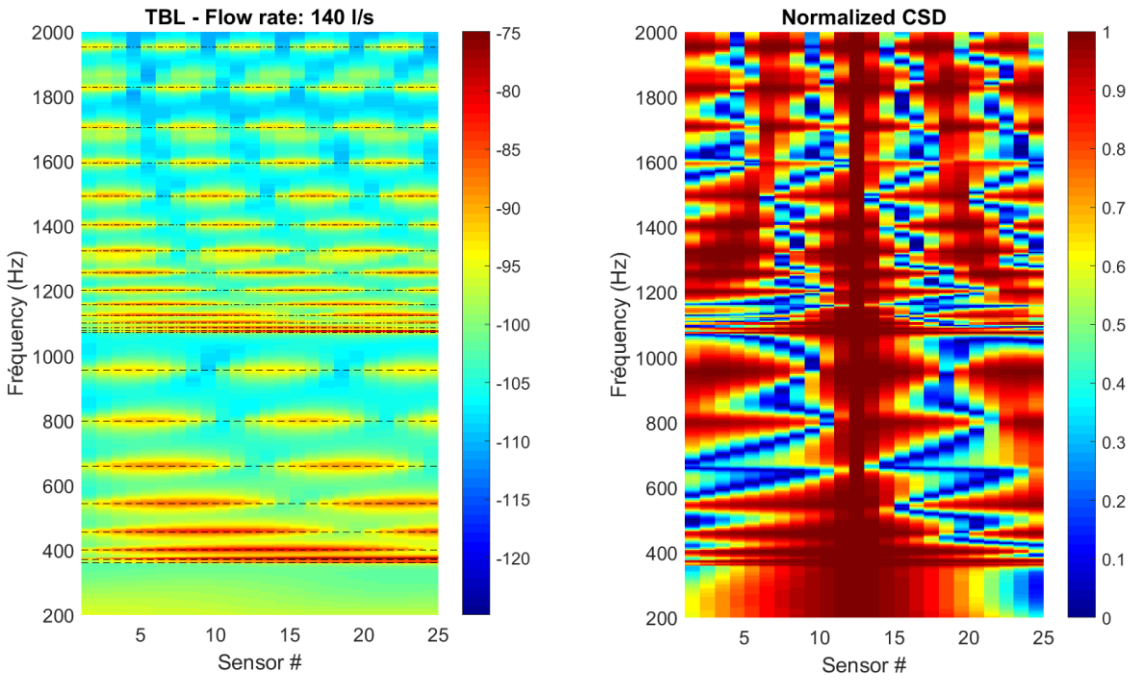

(a) (b)

Figure 4. Analysis of the background noise signals for a flow rate of 140 l s^{-1}: (a), ASD of the accelerations in dB (ref. 1 µm.s^{-2}.$Hz^{-0.5}$) as a function of the sensor number and frequency (The frequencies of the axial modes are indicated with dashed lines); (b), Normalized acceleration CSD between sensor #12 and all the other ones as a function of the sensor number and frequency.

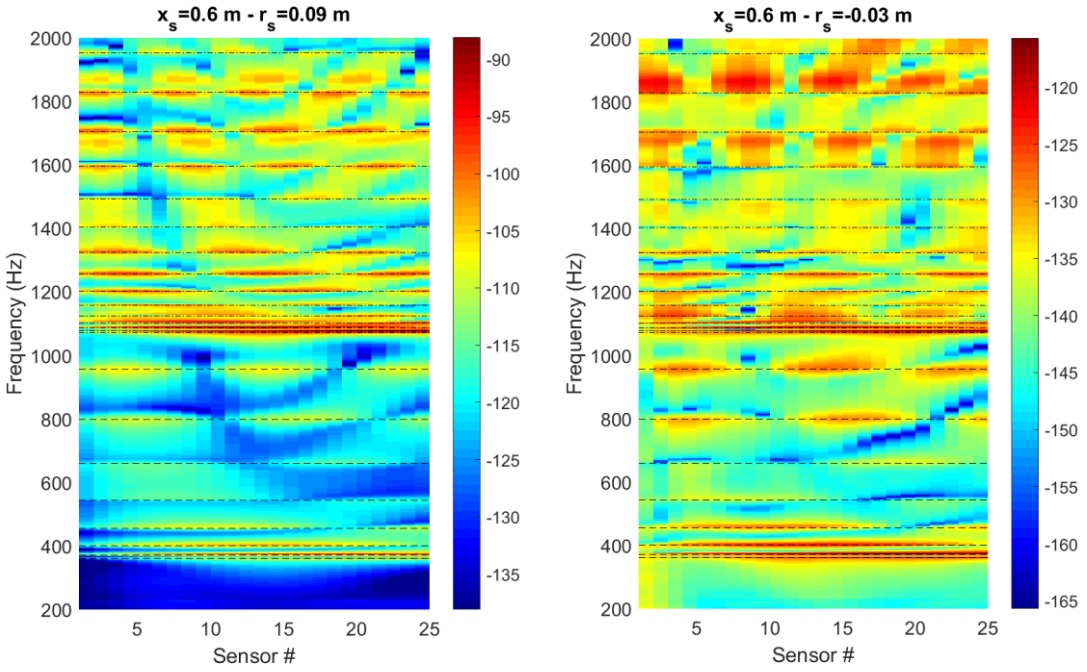

Figure 5. Analysis of the source signals for two source positions: (a), $(x_s, r_s) = (0.6, 0.09)$ m; (b), $(x_s, r_s) = (0.6, -0.03)$ m. ASD of the accelerations in dB (ref. 1 $\text{m.s}^{-2}.\text{Hz}^{-0.5}$) as a function of the sensor number and frequency. The frequencies of the axial modes are indicated by dashed lines.

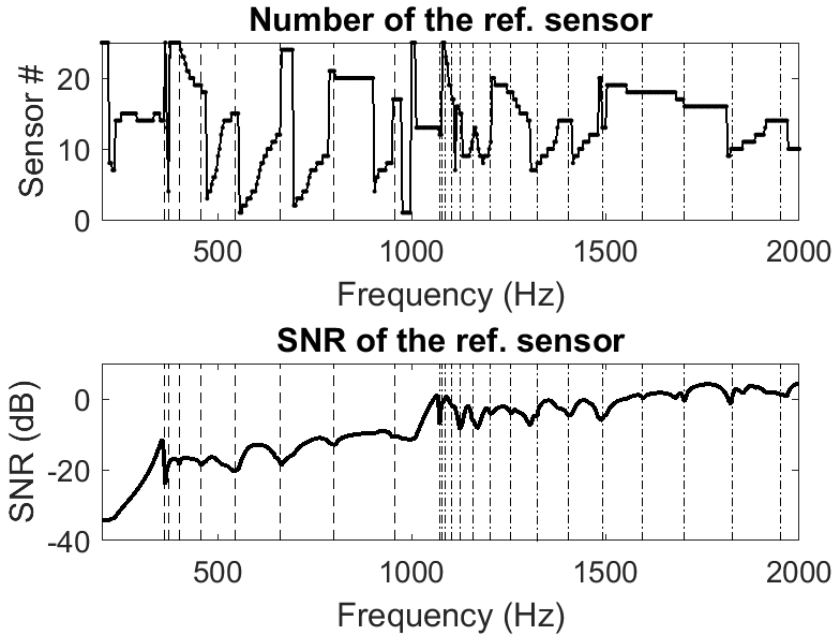

(a)

(b)

Figure 6. (a) Identification number of the reference sensor for each frequency. (b) Signal to noise ratio (SNR) for the reference sensor. Case of an acoustic source at $(x_s, r_s) = (0.6, 0.09)$ m and for a flow rate of 140 l.s^{-1}. The frequencies of the axial modes are indicated by dashed lines.

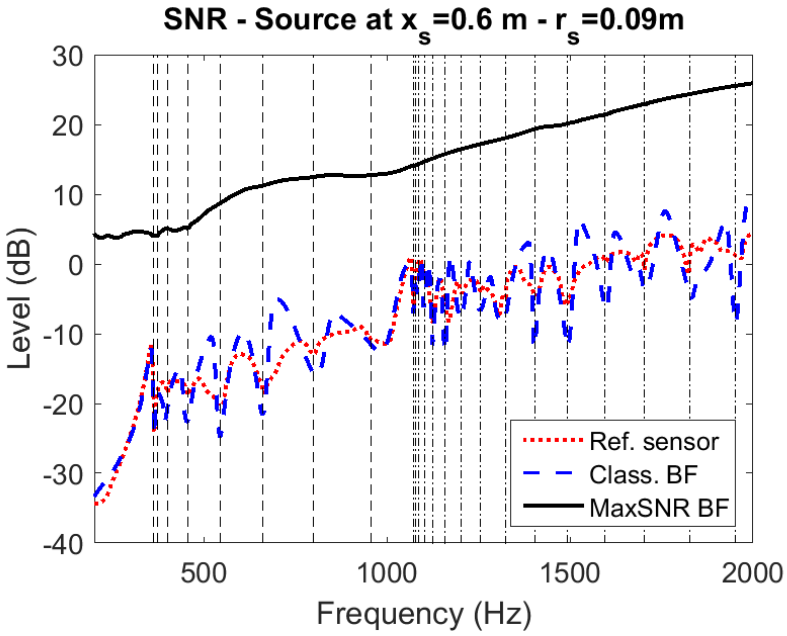

Figure 7. Comparison of the signal to noise ratio (SNR) between the reference sensor, the conventional beamforming and the MaxSNR beamforming. Case of an acoustic source at $(x_s, r_s) = (0.6, 0.09)$ m and for a flow rate of 140 l.s^{-1}. The frequencies of the axial modes are indicated by dashed lines.

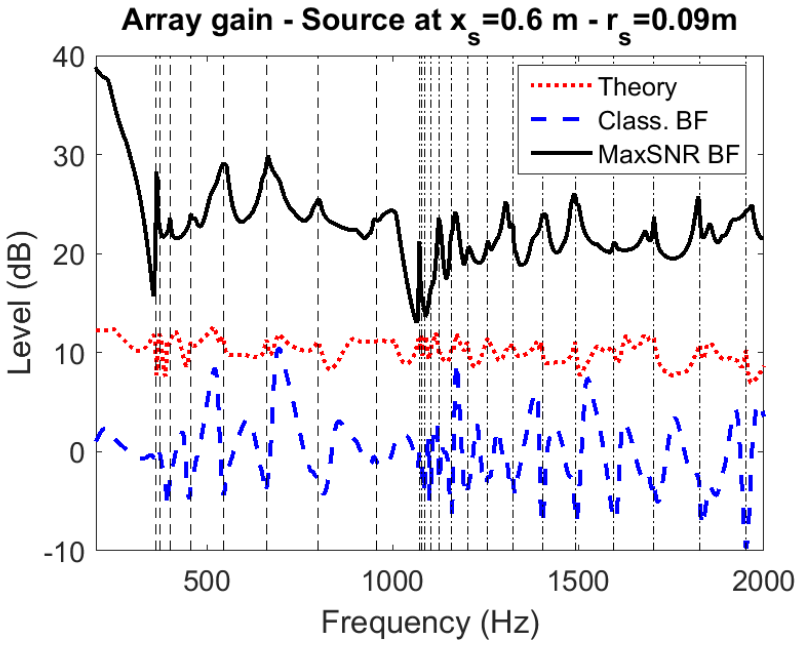

(a)

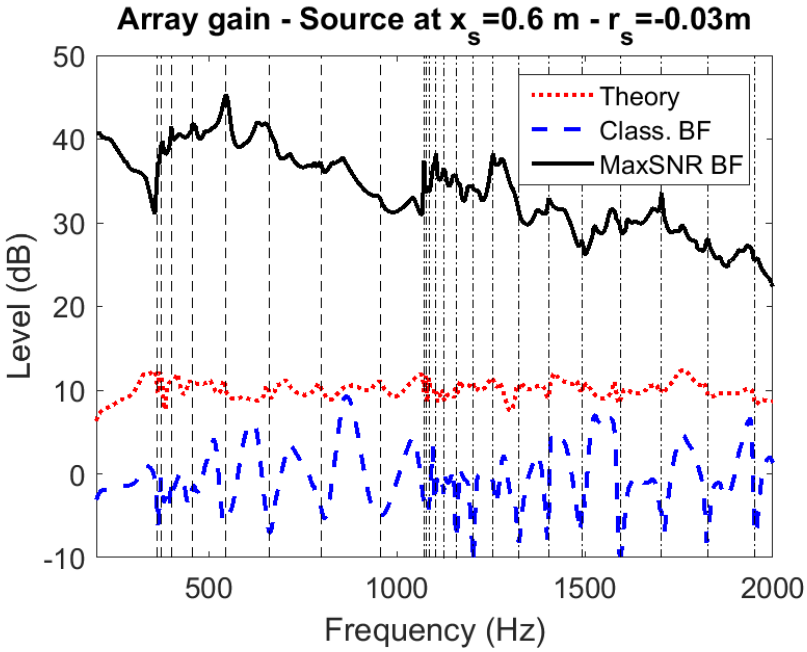

(b)

Figure 8. Comparison of the array gain between the conventional beamforming, the theoretical values for the conventional beamforming assuming uncorrelated noise, and the MaxSNR beamforming. The acoustic source was located at (a) $(x_s, r_s) = (0.6, 0.09)$ m; (b) $(x_s, r_s) = (0.6, -0.03)$ m. The frequencies of the axial modes are indicated by dashed lines.

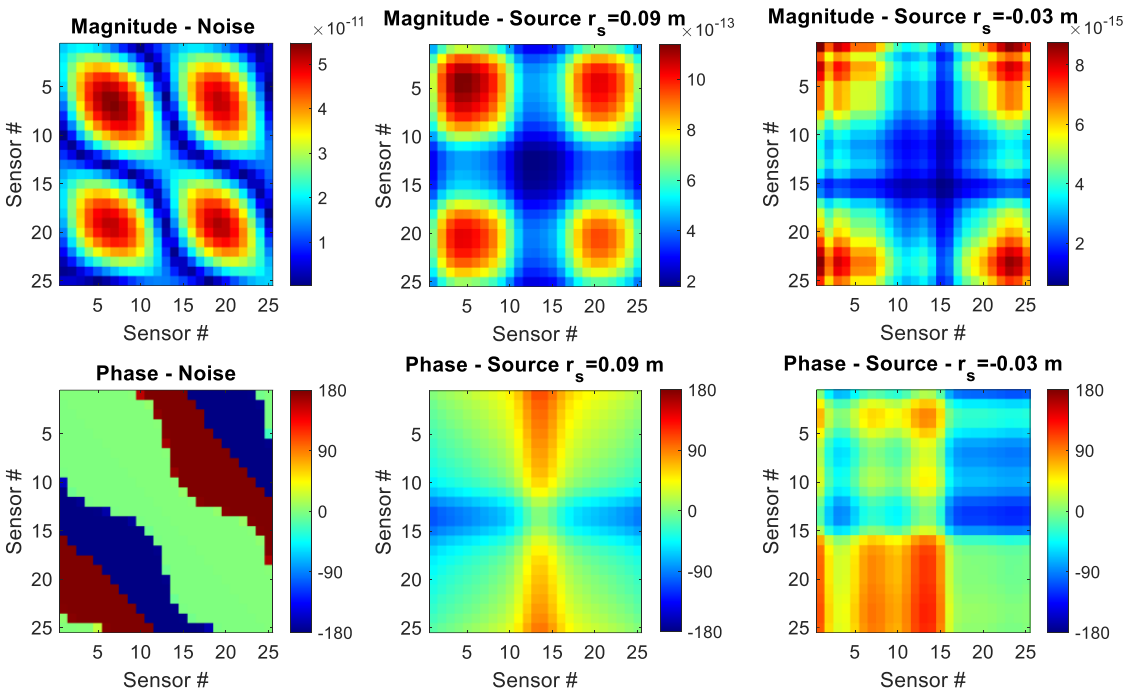

(a) (b) (c)

Figure 9. Analysis of the cross-spectral matrices of the radial accelerations for excitations at 700 Hz by: (a) a turbulent boundary layer with a flow rate of 140 $l.s^{-1}$; (b) an acoustic point source at $(x_s, r_s) = (0.6, 0.09)$ m; (c) an acoustic point source at $(x_s, r_s) = (0.6, -0.03)$ m. The first and second rows show the magnitude ($m^2.s^{-4}.Hz^{-1}$) and phase (°) of the radial acceleration, respectively.

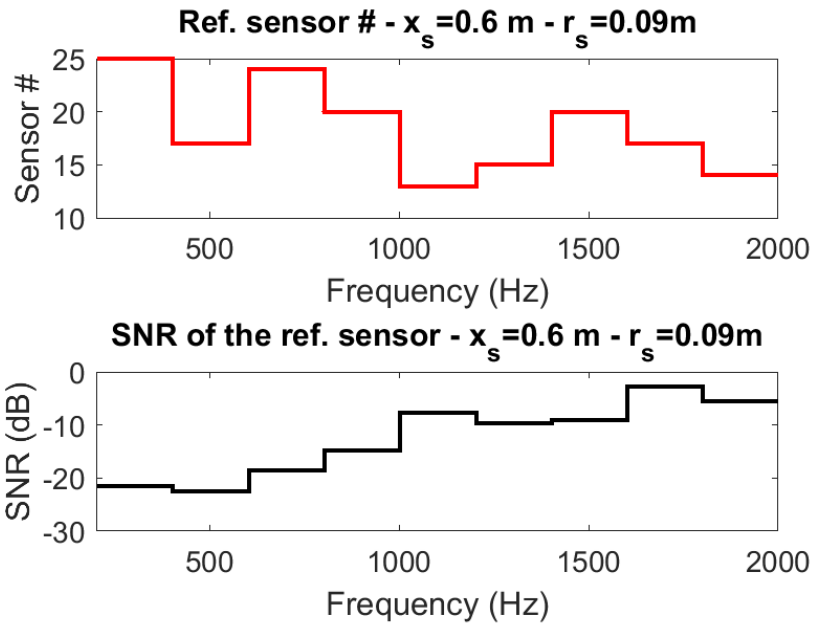

(a)

(b)

Figure 10. Broadband analysis of 200 Hz bandwidth for an acoustic source at $(x_s, r_s) = (0.6, 0.09)$ m and for a flow rate of 140 l.s^{-1} (a) Identification number of the reference sensor; (b) Signal to noise ratio for the reference sensor.

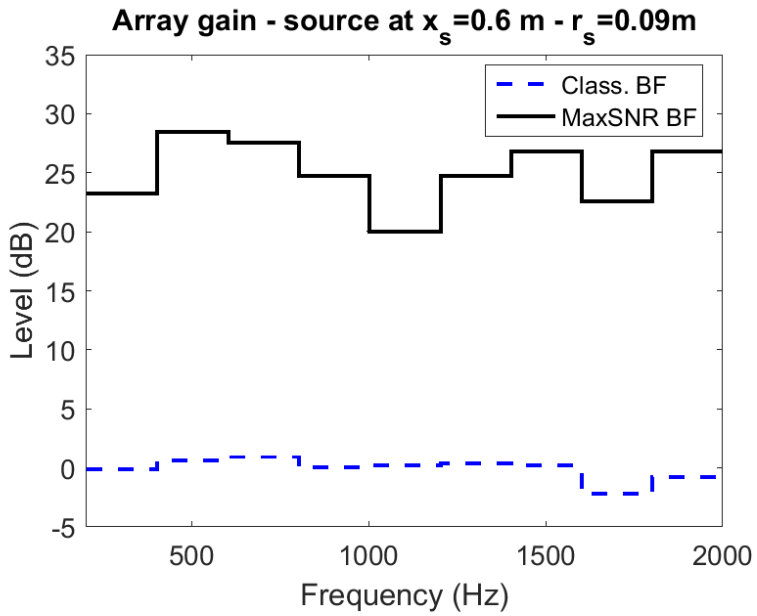

(a)

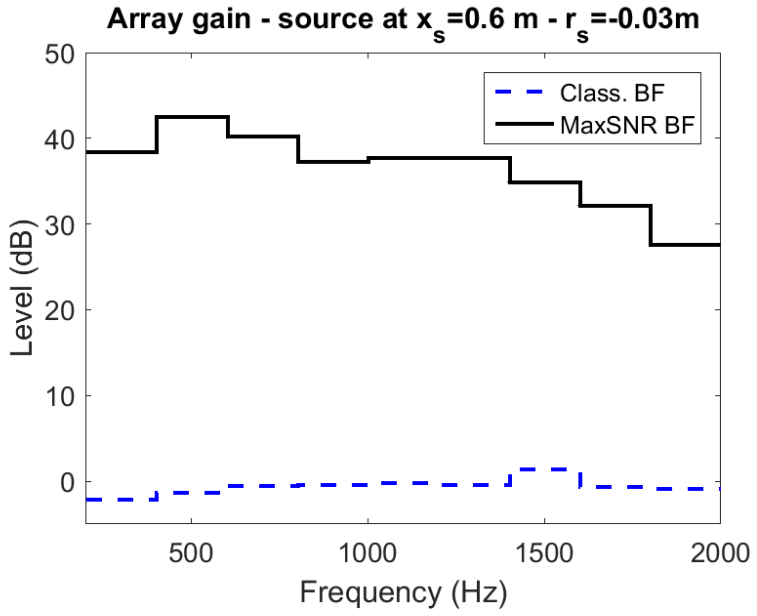

(b)

Figure 11. Broadband analysis comparison of the array gain of the conventional and MaxSNR beamforming techniques. The acoustic source was located at (a) $(x_s, r_s) = (0.6, 0.09)$ m; (b) $(x_s, r_s) = (0.6, -0.03)$ m.

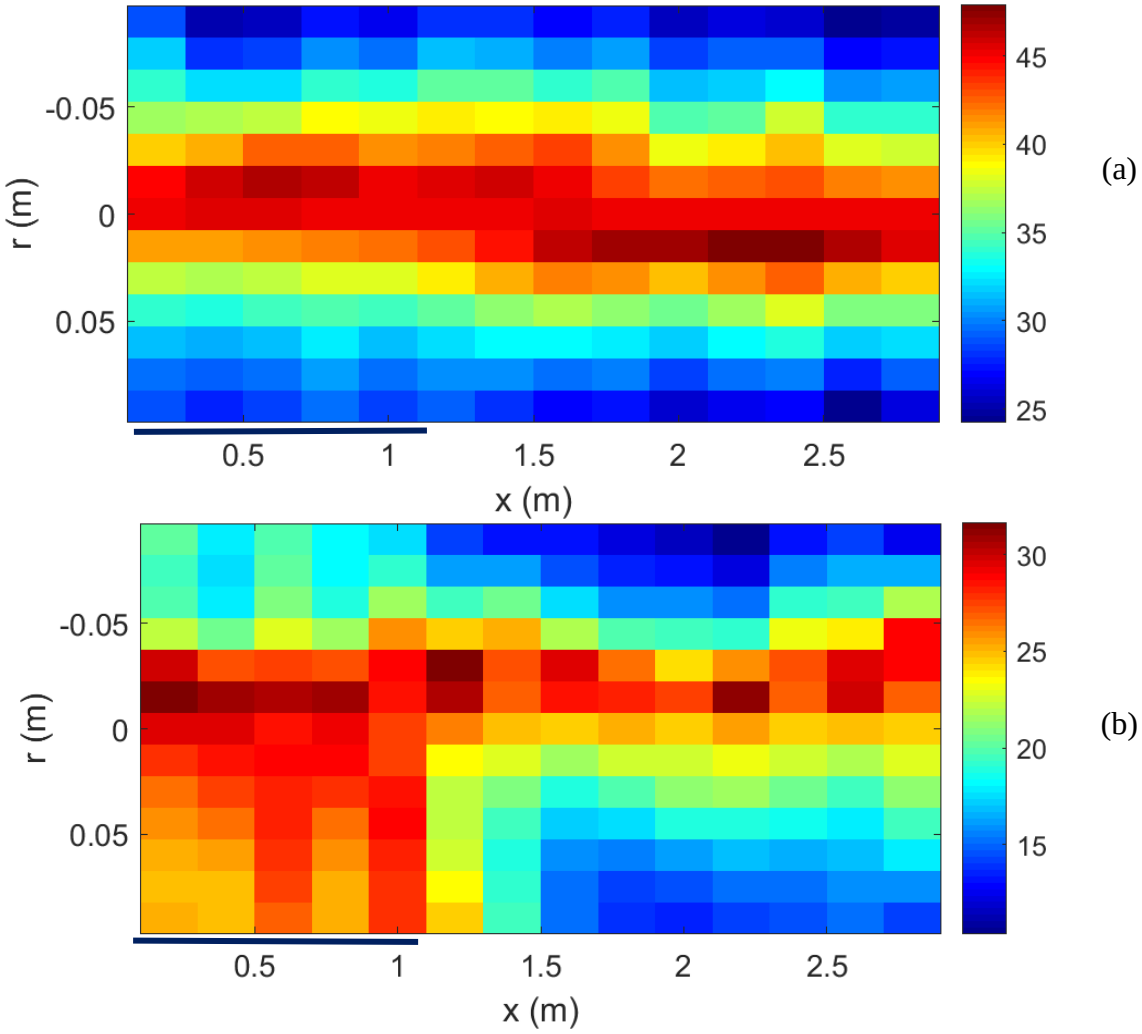

Figure 12. Effective array gain of the MaxSNR beamforming as a function of source position in the detection space in the plane θ=0°: (a) [400 600] Hz; (b) [1800 2000] Hz. The black horizontal line indicates the position of the array.

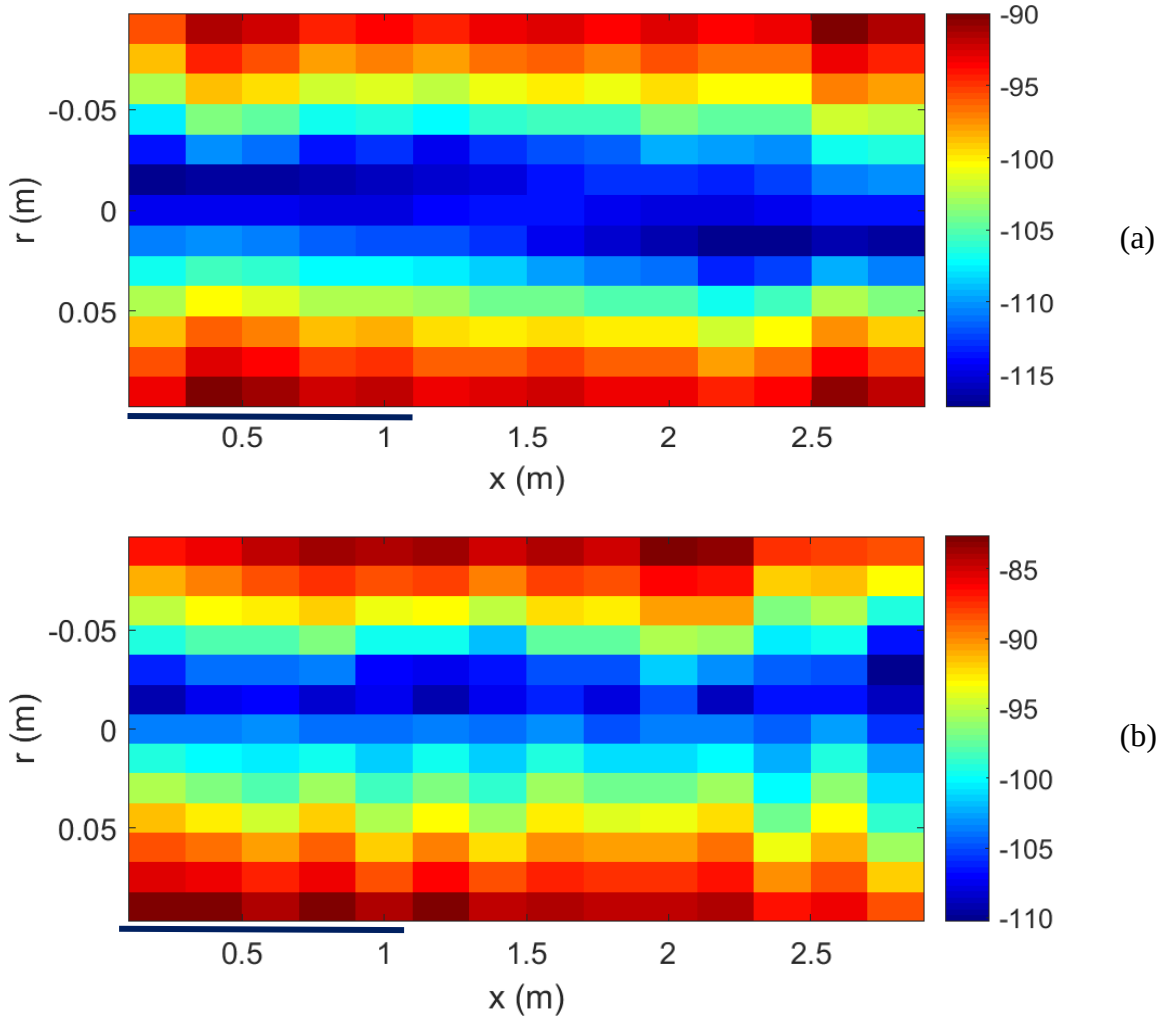

Figure 13. Maximum acceleration measured by the sensors, $\max_{i\in\{1,25\}} \int_{\omega_1}^{\omega_2} S_{ii}(\omega)\, d\omega$ (dB, ref. 1 m.s^{-2}) as a function of the source position in the detection space: (a) [400 600] Hz; (b) [1800 2000] Hz. The black horizontal line indicates the position of the array.

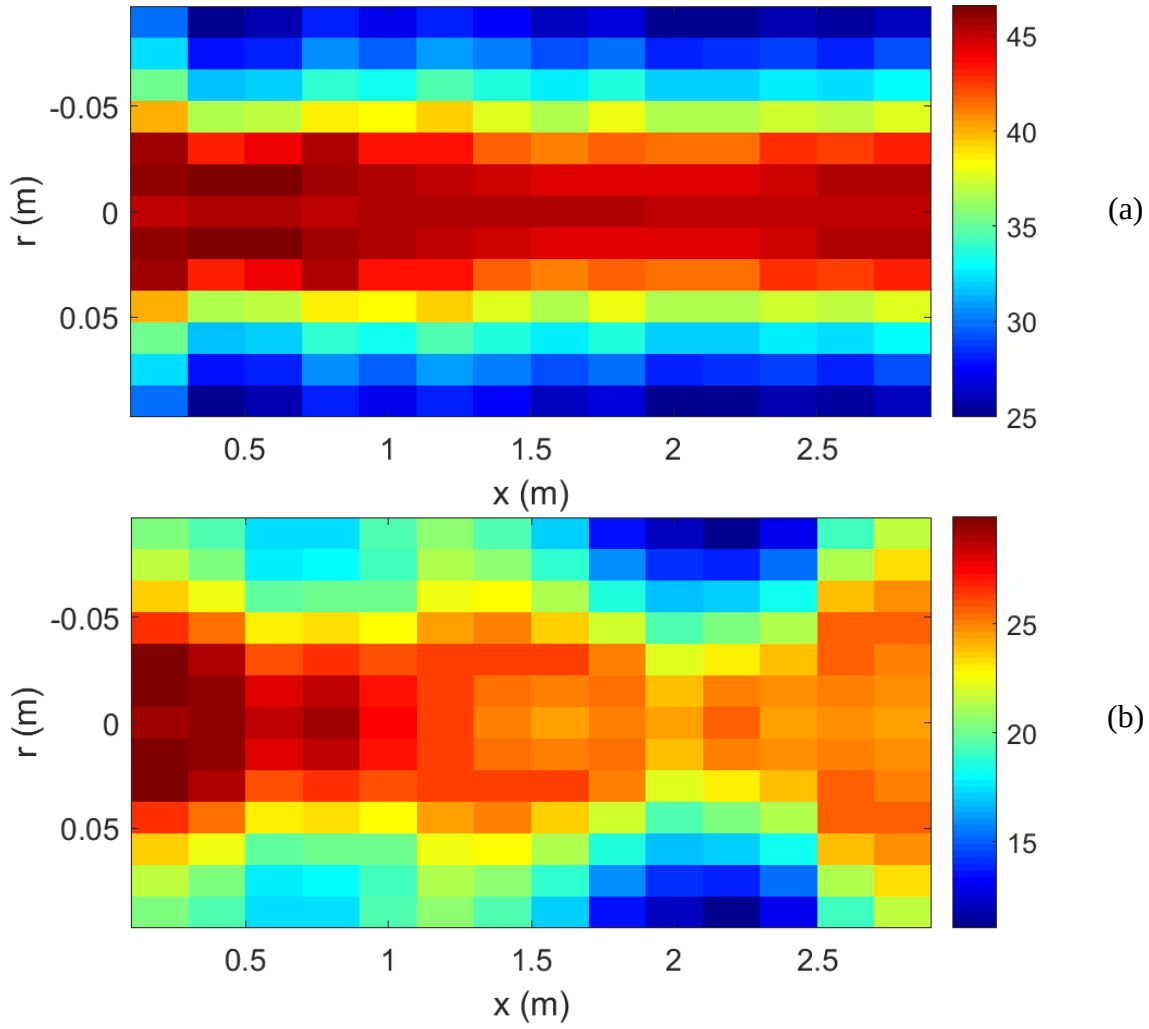

Figure 14. Effective array gain of the MaxSNR beamforming as a function of the source position in the detection space (plane θ=90°): (a) [400 600] Hz; (b) [1800 2000] Hz.

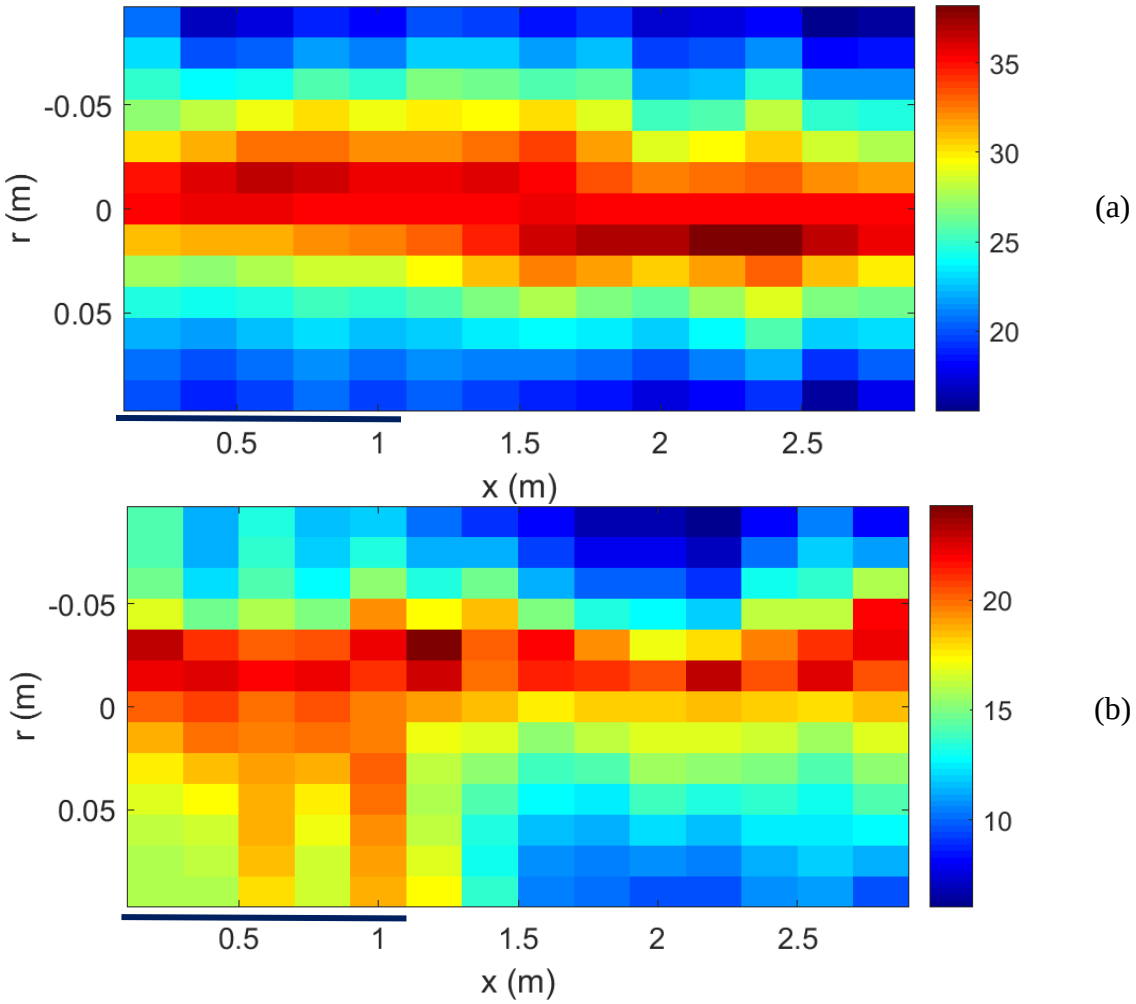

Figure 15. Effective array gain of the MaxSNR beamforming as a function of the source position in the detection space (plane θ=0°): (a) [400 600] Hz; (b) [1800 2000] Hz. Damping loss factor of 1% for the stainless steel and water. The black horizontal line indicates the position of the array.

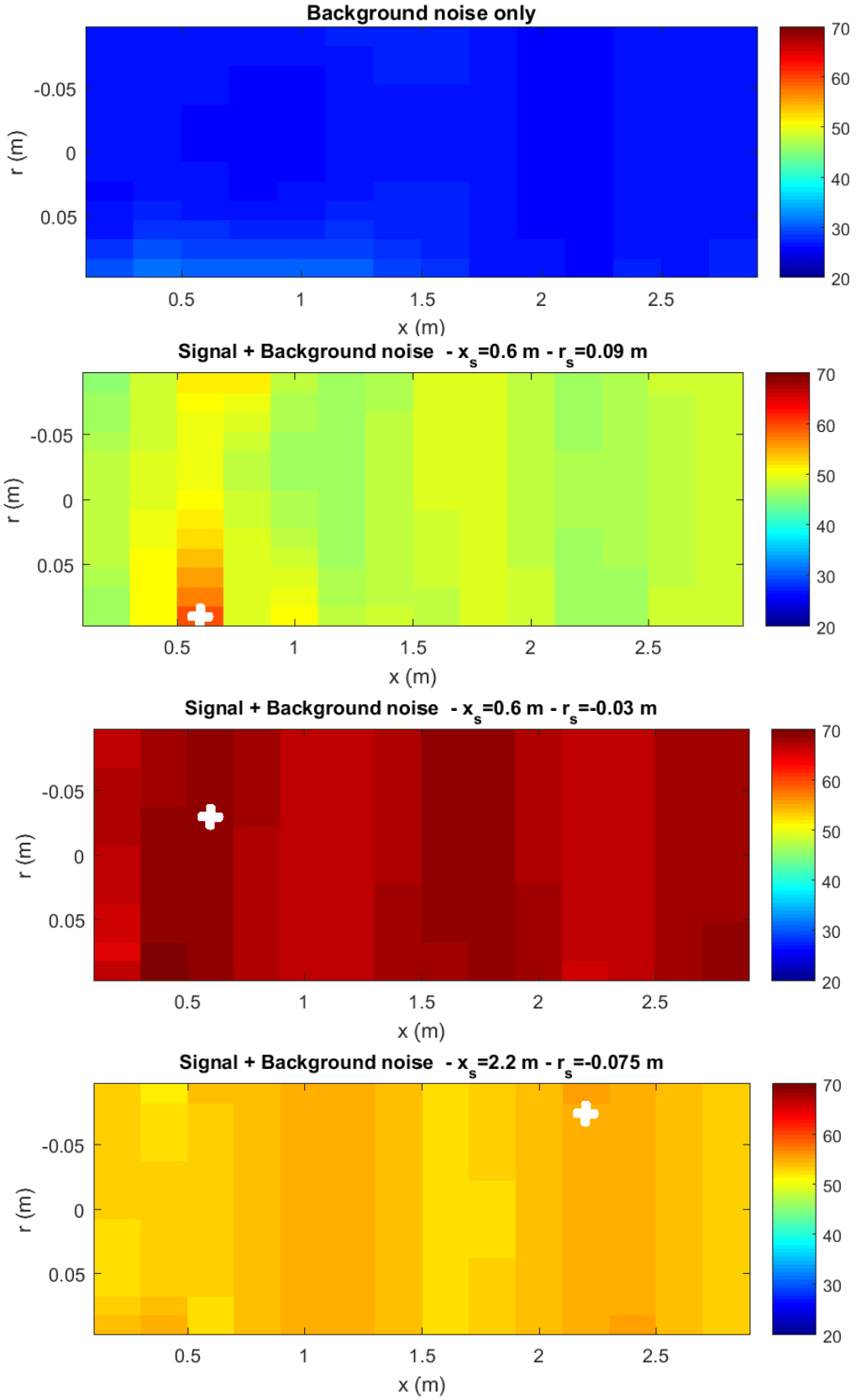

Figure 16. Level (dB) of the MaxSNR beamforming output in the detection space for the frequency band [200 – 400] Hz: (a) Background noise (BN) only; (b) BN + source at $(x_s, r_s) = (0.6, 0.09)$ m (Gain: 28.5 dB); (c) BN + source at $(x_s, r_s) = (0.6, -0.03)$ m (Gain: 42.5 dB); (d) BN + source at $(x_s, r_s) = (2.2, -0.075)$ m (Gain: 29.1 dB). The white asterisks indicate the source position.

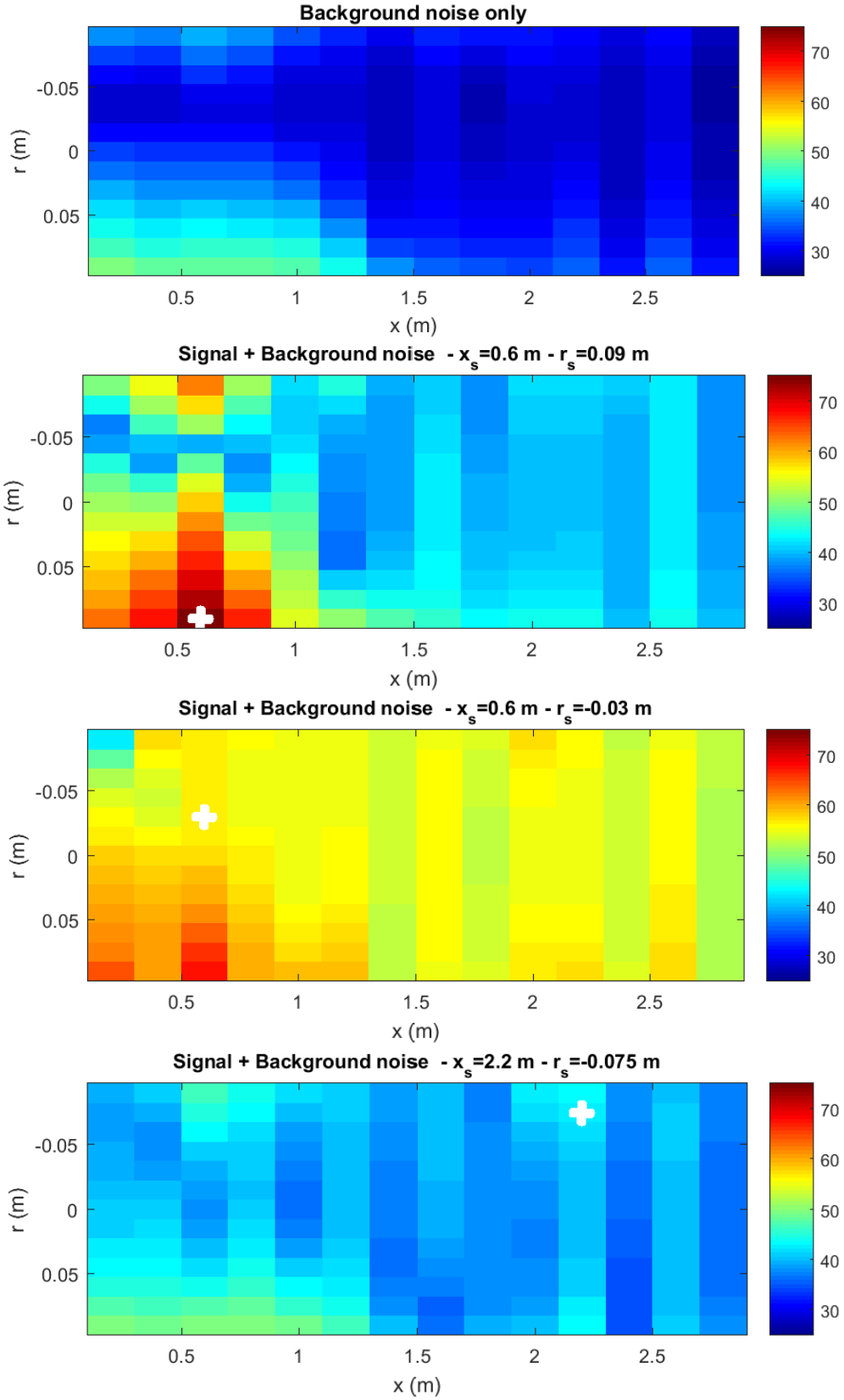

Figure 17. Level (dB) of the MaxSNR beamforming output in the detection space for the frequency band [1800 – 2000] Hz: (a) Background noise (BN) only; (b), BN + source at $(x_s, r_s) = (0.6, 0.09)$ m (Gain: 26.8 dB); (c) BN + source at $(x_s, r_s) = (0.6, -0.03)$ m (Gain: 27.6 dB); (d) BN + source at $(x_s, r_s) = (2.2, -0.075)$ m (Gain: 12.3 dB). The white asterisks indicate the source position.